Climatological assessment of the vertically resolved optical and microphysical aerosol properties by lidar measurements, sunphotometer, and in-situ observations over 17 years at UPC Barcelona

Simone Lolli[1,2], Michaël Sicard[2,*], Francesco Amato[1], Adolfo Comeron[2], Cristina Gíl-Diaz[2], Tony C. Landi[3], Constantino Munoz-Porcar[2], Daniel Oliveira[2], Federico Dios Otin[2], Francesc Rocadenbosch[2,4], Alejandro Rodriguez-Gomez[2], Andrés Alastuey[5], Xavier Querol[5], and Cristina Reche[5]

[1]Italian National Research Council CNR-IMAA, 85050 Tito Scalo (PZ), Italy
[2]CommSensLab, Dept. of Signal Theory and Communications, UPC, 08034 Barcelona, Spain
[3]CNR-ISAC, Via Gobetti 101, 40129, Bologna, Italy
[4]Institut d'Estudis Espacials de Catalunya (Institute of Space Studies of Catalonia, IEEC), Barcelona, Spain, E-08034
[5]Institute of Environmental Assessment and Water Research (IDAEA-CSIC), Barcelona, Spain
[*]Now at Laboratoire de l'Atmosphère et des Cyclones, Université de La Réunion, 97744, Saint Denis, France

Correspondence: Simone Lolli (simone.lolli@upc.edu)

Abstract. Aerosols are one of the most important pollutants in the atmosphere and have been monitored for the past few decades by remote sensing and in situ observation platforms to assess the effectiveness of government-managed reduction emission policies and assess their impact on the radiative budget of the Earth's atmosphere. In fact, aerosols can directly modulate incoming short-wave solar radiation and outgoing long-wave radiation and indirectly influence cloud formation, lifetime, and precipitation. In this study, we quantitatively evaluated long-term temporal trends and seasonal variability from a climatological point of view of the optical and microphysical properties of atmospheric particulate matter at the Universitat Politècnica de Catalunya, Barcelona, Spain, over the past 17 years, through a synergy of lidar, sunphotometer, and in situ concentration measurements. Interannual temporal changes in aerosol optical and microphysical properties are evaluated through the seasonal Mann-Kendall test. Long-term trends in the optical depth of the recovered aerosol, the Ångström exponent (AE) and the concentrations of PM_{10}, $PM_{2.5}$ and PM_1 reveal that emission reduction policies implemented in the last decades were effective in improving air quality, with consistent drops in PM concentrations and optical depth of aerosols. The seasonal analysis of the 17-year average vertically resolved aerosol profiles obtained from lidar observations shows that during summer the aerosol layer can be found up to an altitude of 5 km, after a sharp decay in the first km. In contrast, during the other seasons, the backscatter profiles fit a pronounced exponential decay well with a well-defined scale height. Long-range transport, especially dust outbreaks from the Sahara Desert, is likely to occur throughout the year. During winter, the dust aerosol layers are floating above the boundary layer, while during the other seasons they can penetrate the layer. The analysis also revealed that intense, short-duration pollution events during winter, associated with dust outbreaks, have become more frequent and intense since

2016. This study sheds some light on the meteorological processes and conditions that can lead to the formation of haze and helps decision makers adopt mitigation strategies to preserve large metropolitan areas in the Mediterranean basin.

20 *Copyright statement.*

1 Introduction

Aerosols are small particles suspended in the air and can have a significant impact on both human health and the environment. These short-lived forcers have a brief atmospheric lifetime, typically a few days to a few weeks, and they play a crucial role in shaping the Earth's climate and air quality. These particles come from a variety of sources, including natural processes such as

25 dust and sea salt and human activities such as burning fossil fuels, industrial processes and agriculture.

The effect of aerosols on human health is mainly through inhalation. Particles can cause respiratory problems, such as asthma and bronchitis, and have been linked to increased rates of heart disease and stroke. Long-term exposure to aerosols has also been associated with lung cancer and other respiratory diseases. The elderly and children, who are more susceptible to respiratory problems, are particularly vulnerable to the negative effects of aerosols (Pope III and Dockery, 2006). In addition,

30 in urban environments, aerosols contribute to modulating the urban heat island effect (Xue et al., 2023) during heatwaves.

Aerosols also have a profound impact on climate because they can directly scatter and absorb solar radiation, influencing the energy balance of the Earth and causing cooling or warming (Crosier et al., 2007; Landi et al., 2021). Natural and anthropogenic emissions have different effects on incoming short-wave (SW) solar radiation and outgoing long-wave (LW) radiation emitted by the Earth's surface. Some aerosols, such as sulfates and marine aerosols, reflect short-wave radiation and cool the surface

35 by increasing the planetary albedo. However, the black carbon aerosol layers absorb the incoming SW radiation, warming the air around them during the day. Dust aerosols can affect both incoming SW radiation and outgoing LW radiation, although to a lesser extent. The cooling effect (at surface) of aerosols is significant in regions with high levels of particulate pollution, such as South Asia and East Asia (Bilal et al., 2019; Yang et al., 2020; Huang et al., 2021) and certain areas of the United States (Tosca et al., 2017). The warming effect is most pronounced in the Arctic, where the concentration of aerosols is relatively low.

40 The presence of aerosols in the atmosphere also has an impact on atmospheric stability, vertical movements, and large-scale circulation. They can also affect regional hydrological cycles and cause significant regional climate sensitivity. In recent decades, industrial human activities have significantly altered the net aerosol radiative effect (RE) at the surface, particularly due to increased anthropogenic emissions.

The Fifth Assessment Report (AR5) of the Intergovernmental Panel on Climate Change (IPCC;Stocker (2014)) highlighted

45 that aerosols have a negative effective radiative forcing (ERF) of -1.3 W/m^2 with respect to the industrial era (1750-2014). Effective radiative forcing due to aerosol-cloud interactions is the largest contributor to total aerosol ERF, -1.0 W/m^2 (medium confidence level), while the rest is due to aerosol-radiation interactions, -0.3 W/m^2. Regarding the Fifth Assessment Report, the estimate of the total aerosol ERF has improved with a higher magnitude and reduced uncertainty. This is supported by

advances in understanding, modeling, and observational analysis. The new Sixth Assessment Report (AR6; (Adler et al.,
2022)) undoubtedly shows that the total aerosol ERF is negative. Compared to previous assessments, the ERF due to aerosol-cloud interactions has increased, but the ERF due to aerosol-radiation interactions has decreased. The total aerosol ERF of 1750-2019 is less certain with a magnitude of -1.1 W/m^2, mainly due to recent changes in emissions. For this reason, it is of paramount importance to quantitatively assess how the optical and microphysical properties changed in the past decades.

The uncertainties inherent in current aerosol emission databases are particularly pronounced for absorbing aerosols such as biomass burning and dust, which is a focus of the present research. Some literature (Cohen and Wang, 2014; Qin et al., 2023) suggests that the emission values of these absorbing aerosols (Wang et al., 2021) derived from remote sensing (referred to as "top-down" approaches) can be significantly higher, ranging from 2 to 4 times, compared to the "bottom-up" methodologies that are predominantly adopted by entities such as the IPCC and in many modeling studies. In particular, the findings of these top-down methodologies align more consistently with data from sunphotometer (e.g. AERONET) (Burton et al., 2012) and lidar networks. This congruence underscores the potential relevance of these top-down datasets to our research outcomes. The granularity of these datasets, both in time and in space, could offer critical insights into phenomena such as extreme events or long-range transportation of aerosols. This is especially relevant when studying cases such as wildfires and events that involve the transport of mixed sources of aerosols, both anthropogenic and dust-related, as investigated in this study, where we quantitatively evaluated changes in aerosol optical and microphysical properties by combining long-term data (2004-2020) in situ concentrations of PM_{10}, $PM_{2.5}$ and PM_1, aerosol optical depth, and the Ångström exponent AE obtained from NASA AERONET (AErosol RObotic NETwork; (Tanré et al., 1998)) sunphotometer network and lidar measurements obtained over the past 17 years at the Universitat Politecnica de Catalunya (UPC) in Barcelona, Spain. These measurements were obtained using a lidar deployed as part of the permanent observational network of EARLINET (European Aerosol Research Lidar Network; (Bösenberg and Matthias, 2003; Pappalardo et al., 2014)), which is dedicated to the study of atmospheric aerosols and clouds as part of the ACTRIS (Aerosols, Clouds, and Trace gases Research Infrastructure), which aims, in fact, to understand the properties and behavior of aerosols and clouds in the atmosphere of the Earth and to use this information to improve air quality and climate models.

Barcelona is one of the main industrialized metropolitan areas of the Mediterranean: a coastal city where air pollution is also exacerbated by the pollution of sea vessels (Mueller et al., 2011). In addition, Catalunya is in the middle of a complex region such as the Mediterranean, where the climate changes faster than in other parts of the world. In fact, according to IPCC AR6 (Ali et al., 2022) and other studies (Nicholls et al., 2008; Lewis et al., 2019), temperatures in the Mediterranean are increasing at a rate of 20% faster than the global average. The region's temperatures have already risen to 1.5 ° C higher than preindustrial levels. In contrast, the global temperature increase has been slower, reaching approximately 1.1-1.3°C. If human greenhouse gas emissions were to stop immediately, the Mediterranean region is expected to experience a temperature increase of 2-4 ° C above 19th century levels by 2100. According to (Cramer et al., 2018), the evidence is clear: the already dry Mediterranean regions are becoming even drier. This is a milestone that the IPCC predicts the Mediterranean region will reach by the end of the century or even sooner. This analysis suggests that climate change at this level will transform large areas of southern Spain into deserts. Scrubber vegetation will replace deciduous forests, which will then move upward, replacing alpine conifer-based

ecosystems. For all the previous reasons, quantifying changes in aerosol loading during the last 17 years can help shed some

85 light on how these short-lived tracers can offset climate changes and help implement future adaptation strategies.

2   Materials and Methods

2.1   Instruments

a) *Lidar*

Light detection and ranging (Lidar) is an optically active remote sensing technique that has been increasingly used in atmo-

90 spheric studies over the past few decades. Lidar measurements can provide valuable information on the vertical distribution of
aerosol, cloud, and gas properties, including their optical and microphysical properties. Lidar measurements have been used
in a variety of atmospheric studies, including monitoring air quality (Lolli et al., 2008, 2019), studying the vertical structure
of clouds (Campbell et al., 2016, 2018; Lolli et al., 2017), and measuring greenhouse gases such as carbon dioxide (Abshire
et al., 2010) and methane (Ehret et al., 2017). The very high spatial and temporal resolution of lidar measurements makes

95 them particularly valuable for studying atmospheric processes on regional and local scales. Various lidar techniques, such as
elastic lidar, Raman lidar (Ansmann et al., 1990; Whiteman, 2003), dial lidar (Browell et al., 1998), Doppler lidar (Lolli et al.,
2013), and high-spectral-resolution laser (HSRL; Grund and Eloranta (1991)), make different assumptions, allowing retrieval
of optical and microphysical properties with varying degrees of accuracy.

Lidar observations are available within the framework of the EARLINET/ACTRIS project, as stated in Section 2.1.1. The

100 lidar instrument, deployed at UPC and part of the EARLINET/ACTRIS project since 2000, is a multiwavelength Raman lidar
using a Nd:Yag laser source, which is much more suitable than other sources such as CO_2 (Ciofini et al., 2003).

The UPC multispectral lidar system, which has eight channels, is the third lidar station conceptually designed at the Remote
Sensing Laboratory since the beginning of lidar research in 1993. The station is classified as a $3\beta+2\alpha+1WV+2\delta$ elastic/Raman
aerosol/water-vapor system. The laser source is a pulsed Nd:YAG (350 mJ per pulse) that emits simultaneously at the 1064-nm

105 (near-infrared, NIR) and 532-nm (vis) wavelengths. The system has 8 channels:

- 3 elastic channels (355, 532- and 1064-nm wavelength)

- 3 Raman channels (two channels, 387 and 607-nm wavelength in response to N2 532-nm excitation and one channel,
  407-nm in response to water vapor 532-nm excitation)

- 2 depolarization channels (355 and 532 nm wavelength).

110 The lidar is then able to retrieve the aerosol profile of the particles at the three fundamental harmonics of 355, 532 and 1064
nm.

b) *Sunphotometer*

Sun photometers are powerful passive remote sensing instruments that measure the optical and microphysical properties integrated into the atmospheric column of aerosols. These instruments work by measuring the intensity of direct solar radiation at different wavelengths, allowing us to estimate atmospheric aerosol loading, optical properties, and their size distribution.

In this study, we used data from the Aerosol Robotic Network (AERONET;Holben et al. (1998)) station deployed at the North Campus of the UPC and located in conjunction with the lidar instrument (41.38N, 2.11E, 125 m above sea level).

c) *PM sensor*

The hourly concentrations measured in $\mu g\ m^{-3}$ of PM_{10}, $PM_{2.5}$ and PM_1, corrected by gravimetry (Charron et al., 2004), are taken with the commercially available GRIMM OPC (Optical Particle Counter), which is an instrument used to measure the size and number of particles in the air. This measurement was obtained by continuously sampling the air and counting the number of particles that passed through the instrument's optical sensor.

Data for this study are obtained from the observational site deployed at CID (Center d'Investigació i Desenvolupament) CSIC (Consejo Superior de Investigación Cientificas) in Barcelona (43.38N, 2.11E, 77 m above sea level). All the measured variables, with specifications and references, are reported in Table 1.

2.1.1 Networks of instruments

a) *EARLINET*

The European Aerosol Research Lidar Network, EARLINET, established in 2000, is the first coordinated aerosol lidar network whose main objective is to provide a comprehensive, quantitative and statistically significant database on the spatial and temporal distribution of aerosols on a continental scale ((Bösenberg and Matthias, 2003); (Pappalardo et al., 2014)). Currently, the network includes 31 active stations spread across Europe (Pappalardo et al., 2014). Lidar observations within the network are performed on a regular schedule of one daytime measurement per week around 12 solar times, when the boundary layer is usually well developed, and two nighttime measurements per week, with low background light, to perform Raman extinction measurements. In addition to routine measurements, further observations are devoted to monitoring special events such as desert dust outbreaks, for example (Ansmann et al., 2003); (Mona et al., 2006); (Papayannis et al., 2008); (Guerrero-Rascado et al., 2008); (Mamouri et al., 2013); (Nisantzi et al., 2015), forest fires, for example (Müller et al., 2005); (Amiridis et al., 2009); (Alados-Arboledas et al., 2011), (Nisantzi et al., 2014), photochemical smog (Carnuth et al., 2002) and volcanic eruptions, for example (Pappalardo et al., 2004); (Wang et al., 2008); (Mattis et al., 2010); (Ansmann et al., 2010); (Gross et al., 2012); (Papayannis et al., 2012); (Sicard et al., 2012); (Wiegner et al., 2012); (Navas-Guzmán et al., 2013); (Pappalardo et al., 2013). EARLINET started correlative measurements for the spaceborne lidars on board NASA's CALIPSO (Cloud-Aerosol Lidar and Infrared Pathfinder Satellite Observation) in June 2006 (Pappalardo et al., 2010) and ESA's AEOLUS in August 2018. EARLINET is currently a key component of the ACTRIS infrastructure, which represents a great step toward better coordination of atmospheric observations in Europe towards the establishment of the European component of an Integrated Atmospheric Global System as part of GEOSS, the Global Earth Observation System of Systems (Lautenbacher, 2005). EARLINET is also a contributing network to the Global Aerosol Watch Program of the World Meteorological Organization.

The Barcelona lidar station has been a member of EARLINET since its inception in 2000. The Barcelona lidar group at CommSensLab-UPC has been developing lidar instruments since 1993. The present system has just been updated with a new laser in June 2022. The general characteristics appear in (Rodríguez-Gómez et al., 2022). The system currently has 3 elastic channels (UV, VIS, IR), 2 Raman channels using the pure rotational Raman effect (UV, VIS), 2 depolarization channels (UV, VIS), and 1 water vapor channel. The implementation of a new broadband fluorescence channel is ongoing.

For this study, we used the level 2 backscattering coefficient (quality guaranteed) at 532 nm and 1064 nm. Measurements are taken following the EARLINET measurement schedule, as shown in (Bösenberg and Matthias, 2003) and (D'Amico et al., 2015). The observational site is located on campus north of the UPC at 41.38N and 2.12E, 125 m above sea level.

b) *AERONET*

The NASA Aerosol Robotic Network (AERONET) is a globally distributed network of ground-based sunphotometers operated by academic institutions and government agencies. These are commercially available sunphotometers manufactured by Cimel Electronique (Holben et al., 1998). AERONET has become a critical tool for studying aerosol properties, as the network provides long-term high-quality measurements that can be used to validate satellite observations and improve our understanding of aerosol impacts on the environment. AERONET database is openly available to the public and is widely used by researchers, government agencies, and other stakeholders around the world to inform policy decisions and advance scientific understanding of the Earth system. The success of AERONET can be attributed to the standardization of instrumentation, measurement protocols, and data processing algorithms, which ensure the quality and consistency of the data collected by the network.

2.2 Retrieval Methods

2.2.1 Optical properties

a) *The atmospheric backscatter profile by Raman lidar*

The main advantage of Raman lidar is that it can independently retrieve vertically resolved backscatter and extinction coefficients without assuming an approximate range-independent lidar ratio, i.e., the ratio between the aerosol extinction coefficient and the aerosol backscatter coefficient, which shows very large variability for aerosols (20sr-120sr; (Ackermann, 1998)). Multiple studies (Ferrare et al., 2006; Reichardt et al., 2012) have demonstrated that the precision of the optically resolved vertical properties of the aerosol obtained from Raman lidar is significantly influenced by the solar background. Therefore, to improve their accuracy, measurements are performed primarily at night.

In this study, we use the Raman lidar inversion algorithm of Ansmann et al. (1990) to independently retrieve the vertical profile of aerosol extinction and aerosol backscatter at the elastic wavelength λ_0 (λ_0=355, 532 nm), and hence the aerosol lidar ratio profile given the Raman backscattered lidar return at λ_R (λ_R=387, 607 nm, respectively). Here, λ_R denotes the Raman-shifted wavelength associated with the elastic wavelength λ_0.

The lidar backscatter profiles have a vertical resolution of 60 meters and are averaged seasonally (see Section 3.1 and Section 3.2). However, it is important to note that the lidar database is not uniform across all years. Some periods have more measurements than others, which affects the level of uncertainty associated with the different average profiles. The seasonal Mann-Kendall test (see Section 2.3.2) accounts for these differences in measurement frequency by weighting the averaged profiles accordingly.

b) *Aerosol optical depth*

Another fundamental parameter linked to the aerosol optical properties, the aerosol optical depth (AOD), is a measure of the attenuation of light due to the presence of aerosols in the atmosphere, and can be retrieved both by lidar, by integrating the extinction lidar profile over the altitude, and by sunphotometer, by measuring the amount of direct sunlight that reaches the Earth's surface and comparing it to the amount of sunlight that would have reached the surface if there were no aerosols in the atmosphere. To retrieve the AOD, a sunphotometer typically takes measurements of the solar irradiance at several wavelengths.

The measurements are then used to calculate the AOD by applying the Beer-Bouger-Lambert law (Beer, 1852), which describes the intensity of a laser beam propagating in an inhomogeneous medium (the atmosphere) in relation to the total extinction coefficient (i.e. scattering + absorption), and hence to the aerosol presence. In Table 1 all the different optical and microphysical variables measured by lidar, sunphotemeter, and in situ sensors with relative specifications are reported. The other variables are retrieved from the main variables in Table 1.

Instrument	Measured Variables	Specs	Accessory References
Lidar	Backscatter profile ($m^{-1}sr^{-1}$)	Sicard et al. (2009); Kumar et al. (2011); Zenteno-Hernández et al. (2021)	Ansmann et al. (1990)
Lidar	Volume depolarization profile	Sicard et al. (2009); Kumar et al. (2011); Zenteno-Hernández et al. (2021)	Cairo et al. (1999); Freudenthaler et al. (2009)
Sunphotometer	Aerosol Optical Depth, Ångstrom Exponent	Holben et al. (1998)	Eck and Holben (1999); Dubovik et al. (2002)
Sensor	PM_{10}, $PM_{2.5}$ and PM_1 conc. ($\mu g\ m^{-3}$)	Reche et al. (2022)	Charron et al. (2004)

Table 1. Remote sensing and in situ instruments and the main relative measured variables used for this study

2.2.2   Microphysical properties

a) *Color ratio*

When comparing backscattered signals from two different wavelengths, lidar can distinguish between coarse and fine modes of aerosols, providing important information on their size (Vaughan, 2004; Liu et al., 2017). Coarse mode aerosols are generally larger than 1 micrometer (μm) in diameter and include particles such as dust (Landi et al., 2021), pollen (Sicard et al., 2021) and sea salt. These aerosols are typically emitted from natural sources, such as deserts, oceans, and vegetation, as well as anthropogenic sources, such as construction sites and agriculture.

Fine-mode aerosols are generally smaller than 1 μm in diameter and include particles such as sulfate, nitrate, ammonium, organic carbon, and black carbon. These aerosols are typically emitted from anthropogenic sources, such as fossil fuel combustion, biomass burning, and industrial processes, as well as from natural sources such as volcanoes and wildfires. They often

exhibit complex mixtures, particularly when they are not sourced locally. It is noteworthy that smaller particles, specifically those under 2 μm, showcase this complexity vividly. These particles, often born as carbon-centric cores that, over time, get enveloped by both organic and inorganic layers, forming shells around them. In certain observed cases, there is even evidence that dust particles become coated with anthropogenic pollutants. Such interactions can be particularly relevant in instances where collisions occur between dust and human-induced sources. Analyzing these particle structures using a core/shell framework, or other Mie scattering-based mixing methodologies, aligns with practices already employed by AERONET. Consequently, adopting such an approach in the research presented here would likely produce results consistent with the existing literature and observations

The aerosol backscatter coefficient at a wavelength of 1064nm, obtained from the ACTRIS/EARLINET UPC lidar, is used to determine the aerosol size together with the aerosol backscatter coefficient at 532 nm. Shorter wavelengths (such as 532 nm) are more sensitive to the aerosol fine mode, whereas longer wavelengths (such as 1064 nm) are more sensitive to the aerosol coarse mode. Therefore, the color ratio is often used to differentiate between the coarse and fine modes of aerosols. The color ratio (CR) is defined at each altitude z as the ratio between the backscatter coefficient at 1064 nm $\beta_{1064}(z)$ and the backscatter coefficient at 532 nm $\beta_{532}(z)$ are the backscatter coefficients at 1064 and 532 nm at altitude z.

The color ratio χ is typically expected to fall between zero and one. In general, smaller values of the color ratio are indicative of smaller particles, while larger values ($\chi \approx 1$) correspond to larger particles for which geometric optics can provide an adequate approximation of the scattering process. As shown in (Haarig et al., 2018), CR values greater than 0.7 are related to dust aerosols from the Sahara, while CR values lower than 0.5 indicate smaller particles related to anthropogenic emissions. Between these values, it is likely to be a mixture of anthropogenic aerosols and dust aerosols. This observation may suggest the presence of heavily aged anthropogenic or fire-origin aerosols that have persisted in the atmosphere for an extended period. Over time, these aerosols may have gradually increased in size, approaching the boundary between fine and coarse modes.

CR can also be computed from in situ sensors by taking the ratio between PM_{10}, and $PM_{2.5}$ concentrations as shown in (Fan et al., 2021). Again, values close to 1 indicate coarse aerosol, while values lower than 0.5 indicate a predominance of fine aerosol mode.

b) *Ångström exponent retrieval*

Likewise, the Ångström exponent (AE) can differentiate between coarse and fine mode aerosols. It is defined as the slope of the logarithm of the aerosol optical depth (AOD) at two different wavelengths (440-870nm in this study). The most common way to retrieve AE is by measuring AOD at two or more wavelengths using remote sensing techniques such as sun photometry (Dubovik et al., 2002) or satellite-based instruments (Levy et al., 2010). The sunphotometer measures solar irradiance at multiple wavelengths. The AOD is then calculated by comparing the measured solar irradiance with the modeled solar irradiance, assuming a clear sky. The Ångström exponent can be calculated from the AOD measurements at different wavelengths.

The Ångström exponent is an important indicator of the primary size range of columnar aerosols, as the AOD spectral curve is strongly associated with the particle size distribution (Dubovik et al., 2002). Typically, AE falls within the range of 1.3 to

1.7 in urban or continental sites, has lower values between 0 and 0.6 when there is desert dust, and ranges between 0 and 0.35 in the presence of marine particles, as shown in (Hess et al., 1998; Smirnov et al., 2002; Eck and Holben, 1999; Mazzola et al., 2010). In this study, AE is retrieved from 440-870 nm wavelengths. For future studies, it would be valuable to explore the utilization of different metrics to weigh distinct independent wavelengths. This approach could potentially reveal nuanced information about the composition and characteristics of mixed aerosol types.

Aerosol type	AE (440-870 nm)	References
Urban and Continental sites	1.3-1.7	(Hess et al., 1998; Mazzola et al., 2010)
Desert Dust	0-0.6	(Smirnov et al., 2002; Eck and Holben, 1999)
Marine environment	0-0.35	(Smirnov et al., 2002; Eck and Holben, 1999)

Table 2. Typical AE values for different types of aerosols

c) *Lidar volume depolarization ratio*

UPC lidar instrument is also equipped with a depolarization channel at 532 nm (Sicard et al., 2009; Kumar et al., 2011; Zenteno-Hernández et al., 2021). The laser signal emitted is 100% linearly polarized in a direction. The depolarization channel is measuring the backscattered energy in a direction that is perpendicular to the laser polarization, and then the degree of depolarization is measured. In this study, we use the Level 2.0 volume depolarization product, which is the sum of the molecular and particle depolarization. Detailed information on the volume depolarization channel can be found in Kumar et al. (2011) and Zenteno-Hernández et al. (2021). More generally, lidar depolarization processes can be found in Cairo et al. (1999) and Freudenthaler et al. (2009).

d) *Aerosol typing*

Through the lidar volume polarization channel, it is possible to distinguish between different types of aerosol. Dust particles have irregular shapes that cause them to scatter light in a highly depolarized manner. On the other hand, other types of aerosol, such as water droplets or pollution particles, have more spherical shapes and cause less depolarization of scattered light (Freudenthaler et al., 2009; Lolli et al., 2011; Haarig et al., 2018).

Combustion products and anthropogenic aerosols, in general, found mainly in an urban environment or large metropolitan areas, are predominant spherical (Volume Depolarization < 10%), whereas dust particles and ash from volcanic eruptions (especially fresh) show irregular shapes, with a much higher volume depolarization value, as shown in (Haarig et al., 2018). Volume depolarization is defined as the ratio between the total cross-backscatter coefficient and the parallel total backscatter coefficient at 532 nm.

e) *Fine and coarse mode and implication of aerosol microphysics*

260 Using two independent lidar measurements at two different wavelengths allows the differentiation between coarse and fine aerosols, providing important information on aerosol microphysics (Mamouri and Ansmann, 2014). This is because the size of the aerosol particles affects the way they interact with light at different wavelengths. The backscattered signal by fine particles is more sensitive at 532nm than at 1064nm, whereas coarse particles are less wavelength selective, and the difference in backscattering at the two wavelengths is much less with respect to smaller particulate.

2.3 Statistical Methods

2.3.1 Quality assurance screening

To guarantee the highest possible quality of the final products and, at the same time, to ensure the homogeneity of the data from different types of lidar systems, the EARLINET network has implemented a rigorous quality assurance program that all affiliated stations are expected to meet (D'Amico et al., 2015, 2016). The implementation of the quality assurance program has
270 been and still is one of the main activities of the network and is a prerequisite to establish and monitor over time the performance of different Lidar systems that are part of the network. The Quality Control of EARLINET applies to both lidar instruments and analysis algorithms levels. Without the requirements of the quality assurance program, it is not possible to submit data to the data center. Data that do not comply with the EARLINET standards are rejected already in the submission phase. Automatic feedback is provided to the Data Originator reporting all the problems incurred for each rejected file, fostering the prompt
275 resubmission of the data. There are two types of quality control procedures: • Basic quality control (BQC): technical quality control on the submitted product. They are executed to ensure that the product is compliant mainly from a technical point of view with the defined standard. • Advanced quality control (AQC): a series of physical checks applied to the input product. They are executed to assess the quality from a physical point of view of the product. If one or more basic quality controls fail, the submitted product is rejected and detailed feedback is sent to the data source. If the product satisfies the basic quality
280 controls, it is sent in batches to the advanced quality controls. If the input product fails at least one advanced quality control, the product is labeled as Level 1 otherwise Level 2. Level 1 data are intended as data that users should treat with caution considering failed QC procedures. Information on the result of the QC procedure is reported in the file itself for complete traceability. Level 2 data are, instead, data that are fully compliant with what a user can expect from the ACTRIS/EARLINET network and with data documentation.

285 ### 2.3.2 Year-by-year and seasonal statistical significance

Seasonal Mann-Kendall test

The most suitable way to determine temporal trends in aerosol optical depth (AOD), Ångström exponent (AE), and PM concentrations is through a rank-based non-parametric method, which does not require a specific statistical distribution and can handle missing values, negative or below detection limit values. In this study, the Mann-Kendall (MK) test is used to

identify increasing or decreasing long-term monotonic trends. The Sen slope estimator, which is based on the median of slopes calculated from all possible data pairs, is then used to calculate the slope and confidence limits (95% confidence level in this study). Due to the presence of distinct seasonal patterns in a large number of time series, the modified seasonal MK test (Hirsch et al., 1982) was consistently used to assess trends over 12 months. The MK test is intended for data that are not serially correlated, so the presence of autocorrelation in a time series can affect the results and lead to a higher chance of erroneously rejecting the null hypothesis of no trend. This is known as a type 1 error or false positive. We ran a test on the monthly averaged data without finding any significant correlation (not shown). We then analyze the long-term trends for both AOD and AE retrieved from AERONET and PM_{10}, $PM_{2.5}$ and PM_1 from in situ observation.

Data are aggregated on a monthly average (see below), and seasonal Mann-Kendall (MK) with Sen slope is computed to establish statistically significant temporal trends. MK test takes into account seasonality. The Mann-Kendall test was first proposed as an extension of the Spearman rank (Yue et al., 2002) correlation test. Although Spearman's rho can identify linear relationships between two variables, the Mann-Kendall test can detect both linear and non-linear changes over time. Furthermore, unlike other trend tests, such as least squares regression or analysis of variance, which require large sample sizes for accurate estimates, Mann-Kendall is suitable for small samples that are often encountered in environmental studies (Von Storch and Zwiers, 2002).

For this study, we applied the seasonal Mann-Kendall test in AERONET Version 3 Level 2 quality-checked AOD, AE observations (Giles et al., 2019) and monthly averaged data of Level 2 PM concentration (see Section 3.1). The temporal resolution of the unprocessed AOD, AE, PM, and lidar observations can be found in Table 3.

The seasonal MK test is considered better than other temporal trend tests because of its ability to handle tied data, which can occur frequently in environmental data sets. Additionally, the Mann-Kendall test has greater statistical power than other trend tests, meaning that it is more likely to detect a trend when one exists, and it has a lower Type I error rate, which reduces the chances of falsely detecting a trend when one does not exist.

Variable	Unprocessed resolution	Level 3
AOD	Daily Averages (Giles et al., 2019)	Monthly Averages
AE	Daily Averages (Giles et al., 2019)	Monthly Averages
PMs	Hourly Averages (Reche et al., 2022)	Monthly Averages
Integrated backscatter (0-3 km)	EARLINET Database (D'Amico et al., 2015, 2016)	Seas. Averages (each year)
Integrated backscatter (3-8 km)	EARLINET Database (D'Amico et al., 2015, 2016)	Seas. Averages (each year)

Table 3. Unprocessed temporal resolution of the data and new Level 3 used to determine long-term temporal trends

Average daily AOD and AE values are obtained from the data processing of AERONET level 2 version 3 (Giles et al., 2019). The standard error on the monthly averages is calculated by dividing the standard deviation by the square root of the averaged number of samples, as shown in Eq. 1:

$$\sigma_e = \frac{\sigma}{\sqrt{n}} \tag{1}$$

where σ is the standard deviation from the n measures.

Seasonal Variability

We also checked the seasonal variability of AOD, AE, PM concentrations, and lidar backscatter profiles by averaging the variables and lidar profiles over four seasons, namely December-January-February (DJF), March-April-May (MAM), June-July-August (JJA), and September-October-November (SON). The unprocessed temporal resolutions of the concentrations of AOD, AE, PM are reported in Table 3, while the single-calculus chain (SCC) lidar profiles are quality-assured at Level 2, as reported in Section 2.3.1.

The vertically resolved lidar profiles for backscatter are seasonally averaged strictly following the ACTRIS/EARLINET schedule. Out-of-schedule measurements are ignored to avoid any possible bias due to particular conditions, i.e., biomass burning or dust outbreak.

AOD and AE, even if they are not normally distributed (see Figure 9), if we take more than 30 samples, AOD and AE are approximately normally distributed. Again, the error in mean can be computed by dividing the standard deviation by the square root of the averaged samples.

3   Results and Discussion

Lidar observations, due to the complexity of the instrument and the EARLINET measurement schedule, are much less dense with respect to PM_{10}, $PM_{2.5}$ and PM_1 and AERONET AOD and Ångstrom exponent measurements.

3.1   Long-term aerosol-load concentration trends (2004-2020)

As shown in Figure 1, seasonal MK test with Sen's slope on the concentrations of PM_{10}, $PM_{2.5}$ and PM_1 at the surface level has decreased since 2004 with a statistically significant slope of -1.07 (CI 95% -1.31 -0.82), -0.73 (CI 95% -0.86 -0.59) and -0.68 (CI 95% -0.81 -0.59) μ g m^{-3} per year, respectively. This corresponds to a reduction of 11.5, 9.5 and 8.5 μg m^{-3} in 17 years, which corresponds to a decrease in the concentration of PM_{10}, $PM_{2.5}$ and PM_1 by approximately 54%, 61% and 68% (95% confidence level).
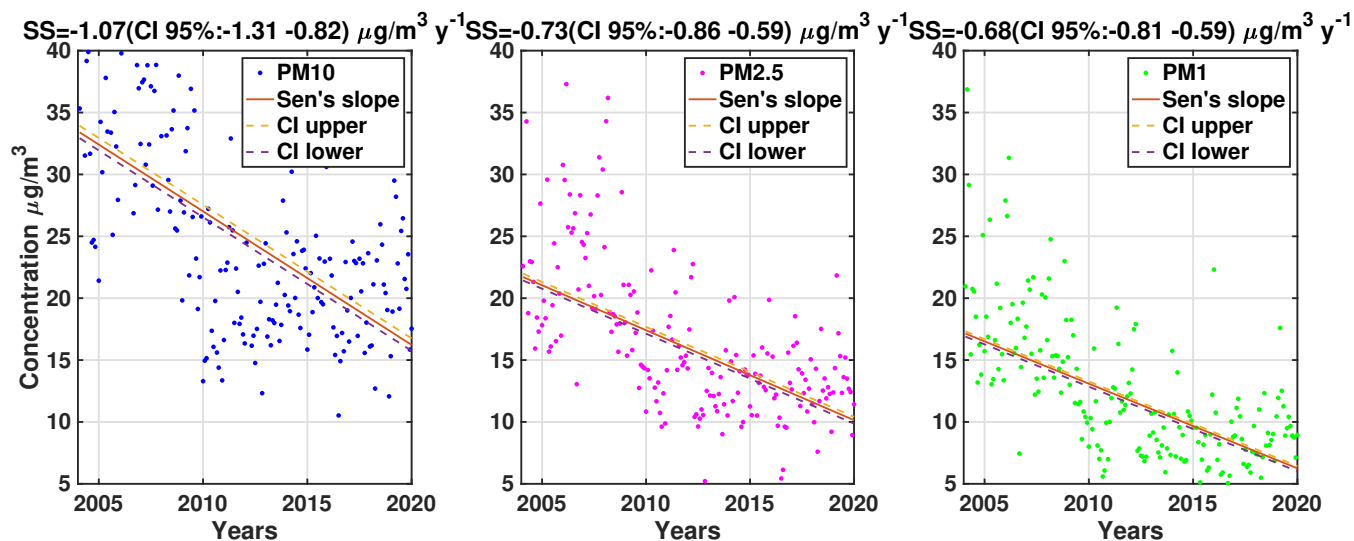
Figure 1. Plot of seasonal MK test for monthly averages of PM_{10}, $PM_{2.5}$ and PM_1. A trend is evident at a confidence level 95% with a Sen slope of -1.07 (CI 95% -1.31 -0.82), -0.73 (CI 95% -0.86 -0.59) and -0.68 (CI 95% -0.81 -0.59) $\mu g \ m^{-3} \ y^{-1}$ respectively. These values correspond to a decrease of 54%, 61%, and 68% over 17 years.

This is an important result that confirms that the reduction policies implemented in recent decades were effective in improving air quality. In fact, PM_1 is much less related to natural pollution episodes compared to PM_{10} and $PM_{2.5}$ concentrations because fossil fuel combustion products are much smaller in size than dust, ash and marine salt outbreaks. However, reduction policies are ineffective in reducing the effects of natural and/or biogenic aerosol outbreaks, such as dust, marine salt, and volcanic eruptions.
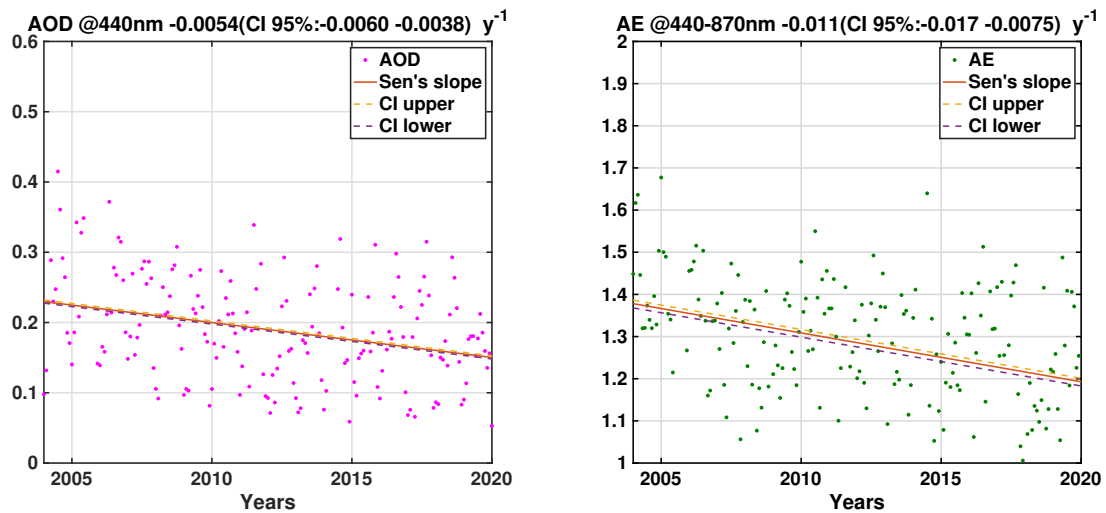
Figure 2. Plot of Seasonal MK test for AOD monthly averages at 440nm and Angstrom exponent from AERONET data. A trend is evident at a confidence level of 95% with a Sen slope of -0.0054 (CI 95% -0.0060 -0.0036) for the AOD and -0.011 (CI 95%:-0.017 -0.0075) for Ångstrom exponent.

The seasonal MK test with Sen's slope applied to monthly AOD averages at 440 nm showed a drop of 37% over 17 years (-0.0054 y-1; CI 95% -0.0060 -0.0038). The decrease in AOD is smaller than the drop in PM because AOD is a columnar value that includes the aerosol layers of the upper troposphere, usually advected from distant sources. For the Ångstrom exponent (AE), the drop in 17 years is 13% (-0.011 y-1; CI 95% -0.017 -0.0075). The drop in the ngström exponent confirms again that the reductions in emission policy were effective, since lower values of AE are related to larger aerosol particles, which in turn are linked to natural emissions such as dust, ash, and marine salt.

Lidar observations are fewer in number compared to those of AOD, AE, and PM because the instrument is much more complex. In this analysis, we apply the seasonal MK test to two parts of the yearly averaged backscatter profiles by season at 532 nm. The lower part of the backscatter, from the ground to the top of the boundary layer (0 km-3 km), and the free troposphere (3 km to 8 km) from 2004 to 2020.
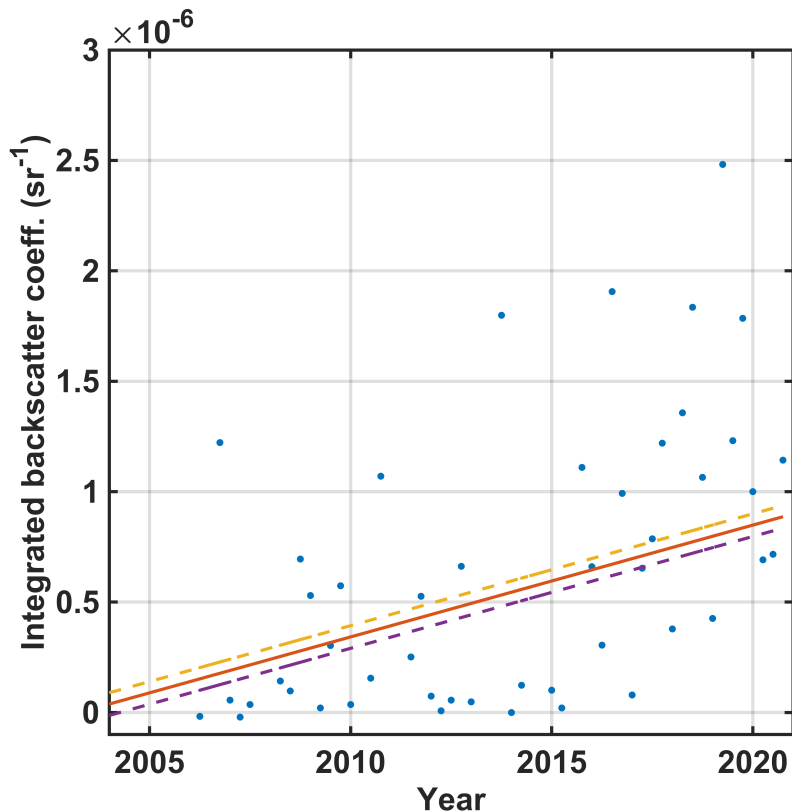
Figure 3. The MK test was applied to the averaged integrated backscatter profiles averaged by season (for each year) from 3 km to 8 km. The Sen slope is 5.48 10-8 $sr^{-1} y^{-1}$ (CI 95%: 2.48 10-8 $sr^{-1} y^{-1}$ - 7.24 10-8 $sr^{-1} y^{-1}$)

In the boundary layer (0 km-3 km), there is no significant trend at the 95% level, while in the free troposphere (3 km - 8 km) the average backscatter coefficient increases at a rate of 5.48 10e-8 $sr^{-1}y^{-1}$ (CI 95% 2.48 10-8 $sr^{-1}y^{-1}$ - 7.24 10e-8 $sr^{-1}y^{-1}$). For this tiny increase, we can then speculate that advected aerosol layers from distant sources, for example, dust outbreaks and biomass burning, have increased in the last 15 years. This speculation is also supported by (Evan et al., 2016). The same trend is not reflected in the boundary layer. This means that the reduction, seen from the sunphotometer and PM sensors, occurs in the first hundreds of meters where the field of view for the laser and telescope of the lidar either do not overlap or only partially overlap, making the measurements unavailable.

3.2 Seasonal climatological analysis on long-term lidar observations

Lidar instruments have higher data collection and processing demands compared to in situ sensors for measuring PM and sunphotometers. Active remote sensing optical devices require more power, calibration, and maintenance to operate correctly, which can lead to data gaps. Additionally, lidar measurements are highly sensitive to atmospheric conditions, such as cloud cover, which can affect their ability to detect aerosols on cloudy days. As a result, lidar observations may be less homogeneous

and some months/years may have more data than others. Consequently, it is very difficult to assess long-term trends with an in-homogeneous database. However, it is possible to quantitatively assess the seasonal variability of the vertically resolved optical properties, which is crucial, particularly from a climatological standpoint. To achieve this result, we considered four seasons: December-January-February (DJF), March-April-May (MAM), June-July-August (JJA), and September-October-November (SON). We obtained four averaged profiles, each representing the atmospheric aerosol load for each season. Profiles are ob-tained by taking the median average of the level 2 backscattering atmospheric profile. We used the median instead of the mean to eliminate the effects of outliers, for example, occasional aerosol plumes caused by land clearing activities by local landown-ers. From 2004 to 2020, lidar quality-assured aerosol backscatter profiles are 2630, both at 532 and 1064 nm. Due to cloud coverage and adverse meteorological conditions, median backscatters are obtained for the fall and winter seasons, averaging a lower number of profiles compared to spring and summer, as shown in Table 4.

Season	Averaged lidar profiles
DJF	338
MAM	981
JJA	935
SON	378

Table 4. Number of averaged lidar profiles by season (2004-2020).

The median average profiles are shown in Figure 4 with relative precision. At first glance, the summer aerosol layer, after a sharp decay in the first km, reaches an altitude of 5 km, while the other backscatter profiles during spring, fall, and winter exhibit a more pronounced exponential decay. During winter, the constant sharp drop of up to 1.7 km suggests aerosol of local origin, while the remaining profiles indicate a higher boundary layer height or upper air aerosol transport (max during summer months).
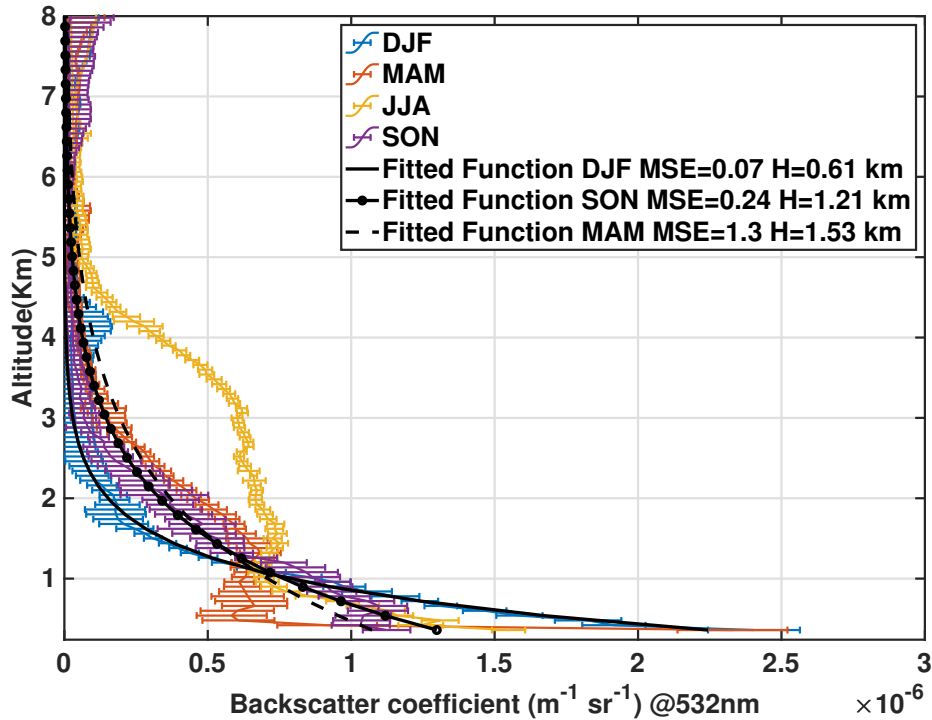
Figure 4. Vertically resolved median backscattering profiles for DJF, MAM, JJA, and SON. Error bars are obtained by computing the standard error (value $\pm\ 1\ \sigma_e$; Eq. 1). The spatial resolution is constant and fixed at 60 m. Black curves: Scale Height Retrieval and Relative Mean Square Error Fitting the backscatter profiles through a monoexponential function]

380   To better characterize the behavior of the backscatter profile, we fit the vertically resolved profiles of Figure 4 with an exponential function:

$$f(x) = A * exp(-\frac{x}{H}) \tag{2}$$

where H is the scale factor indicated in our case at which altitude the backscattering drops by 63% (1/e). The fitted profiles are depicted in Figure 4. The Mean Square Error (MSE) is very small for DJF, the plot showing an almost perfect fit and a
385   scale height H=0.61 km. JJA is not represented because the curve cannot be fitted by an exponential function.

The Iberian Peninsula is also prone to dust outbreaks, especially during certain periods of the year (Sicard et al., 2011, 2012). To assess dust outbreaks, we analyzed the median-averaged depolarization ratio profiles, since dust particles strongly depolarize the lidar signal. For this reason, in Figure 5, the seasonal backscattering coefficient is paired with the seasonal vertically resolved volume depolarization profile at 532nm, still obtained from the EARLINET/ACTRIS Barcelona station.

390   It is important to emphasize that backscatter measurements retrieve optical properties of aerosols, while volume depolarization is related to aerosol microphysical properties. In fact, a peak in the volume depolarization channel indicates the altitude at which the most depolarizing aerosols are found, which is not necessarily related to their concentration.
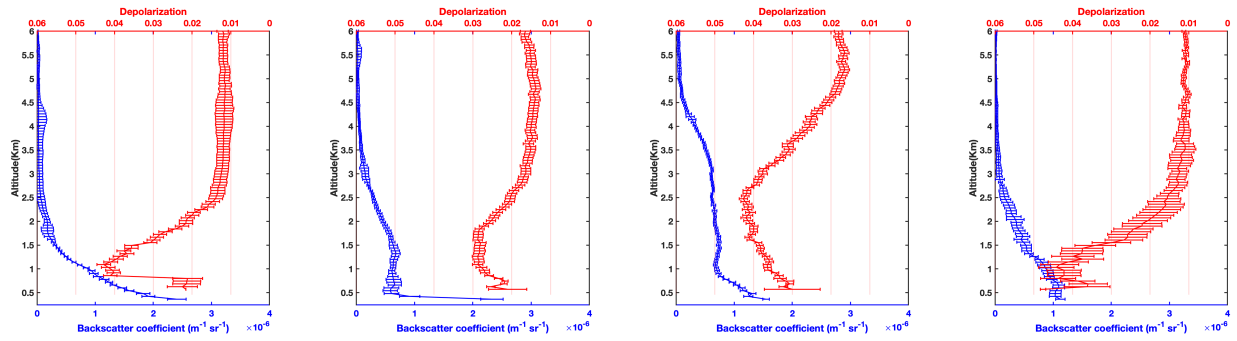
(a) DJF Backscattering coefficient and depolarization.

(b) MAM Backscattering coefficient and depolarization.

(c) JJA Backscattering coefficient and depolarization.

(d) SON Backscattering coefficient and depolarization.
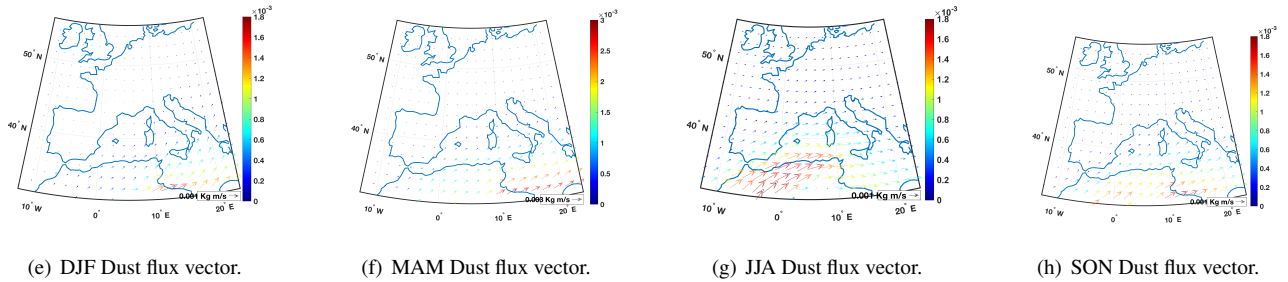
(e) DJF Dust flux vector.

(f) MAM Dust flux vector.

(g) JJA Dust flux vector.

(h) SON Dust flux vector.

Figure 5. DJF, MAM, JJA, SON backscatter and depolarization vertically-resolved profiles at 532 nm. The errorbars are obtained computing the standard error (value $\pm$ 1 σ_e; Eq. 1). The spatial resolution is constant and set at 60 m. Synoptic maps were obtained from Modern era retrospective analysis for research and applications (MERRA; Giovanni (2015)). They represent the columnar dust flux averaged by season from 2004 to 2020.

In Figure 5, the vertically resolved volume depolarization profiles (in red) show significant variability that strongly depends on the season. During winter (Figure 5(a)), there is a sharp volume depolarization peak at around 1 km, while during summer
395 (Figure 5(c)), the curve is mostly flat from the ground up to 2.5 km, where the depolarization reaches a maximum. During spring and fall (Figures 5(b) and 5(d)), the peak is not as sharp as in winter and reaches an altitude of up to 1.5-2 km before starting to decay exponentially. The analysis showed that dust outbreaks are possible during all seasons, but there are fundamental differences.

During winter (DJF), long-range transport of aerosol layers is mostly floating at the top of the boundary layer, without long-
400 range transport in the upper air at higher altitudes. It is also unlikely that dust will be found within the boundary layer. For this reason, during winter, the aerosols in the boundary layer are mainly local in origin and are not influenced by long-range transport. During summer (JJA), the depolarization curve is almost flat, indicating that dust aerosol layers can also be found within the boundary layer. The depolarization peak is found at an altitude of 2.5 km, followed by a sharper drop. The backscatter coefficient (blue) shows the aerosols present up to an altitude of 5 Km. We speculate that long-range biomass-burning aerosol
405 layers are advected toward the region. In fact, biomass burning is present in large part during the summer months, as shown

by (Ancellet et al., 2016). This type of aerosol does not exhibit significant volume depolarization, so it remains undetected by depolarization, but can be detected through backscatter. During the fall, the volume depolarization curve peaks around 1.3 km. The curve is not as sharp as in winter, indicating a possible intrusion of Saharian dust into the boundary layer. During spring, although still probable, the volume depolarization values are 40% lower. Through our detailed analysis, we discerned different seasonal patterns. Specifically, our findings underscore that May exhibits characteristics more similar to those of the summer months (not shown). In terms of aerosol transport dynamics related to biomass burning (BB), data patterns in May align more closely with those observed in the summer months (JJA). This stands in contrast to the earlier spring months, March and April, which displayed markedly different characteristics. Therefore, as highlighted above, the behavior observed in May is more congruent with the summer months, reinforcing the idea that May's atmospheric conditions might be transitioning earlier into summer-like patterns.

Figures 5(e), 5(f), 5(g), 5(h) show the seasonal columnar averaged dust flux from 2004 to 2020 obtained from NASA Geospatial Interactive Online Visualization ANd aNalysis Infrastructure, GIOVANNI Giovanni (2015). As we can observe, the dust flux over Barcelona is stronger during summer (JJA), while it is weaker during winter (DJF). Lidar observations also confirm the results found by (Marinou et al., 2017) using NASA Cloud-Aerosol Lidar and Infrared Pathfinder Satellite Observations (CALIPSO) , where, even if the seasons are offset by a month, show that for Barcelona, latitude dust can be found up to 5 km in summer and 1 km in winter.

In summary, long-range dust outbreaks are likely to occur throughout the year. Volume depolarization values are lower in spring, indicating aged dust or mixing with other aerosol species, such as biomass burning or pollen(Sicard et al., 2021). During winter, the dust aerosol layer floats mostly at the top of the boundary layer, whereas in other seasons it can also be found inside. Most of the dust can be found at 2.5 km during summer (up to 5 km), 1 km during winter, and 1 to 1.5 km during spring and fall. Several studies corroborated this speculation, and a reanalysis of seasonal maps (DJF, MAM, JJA, SON) of dust loading across Europe by the Barcelona Supercomputing Center (BSC) Dream model can be found in (Basart et al., 2012).
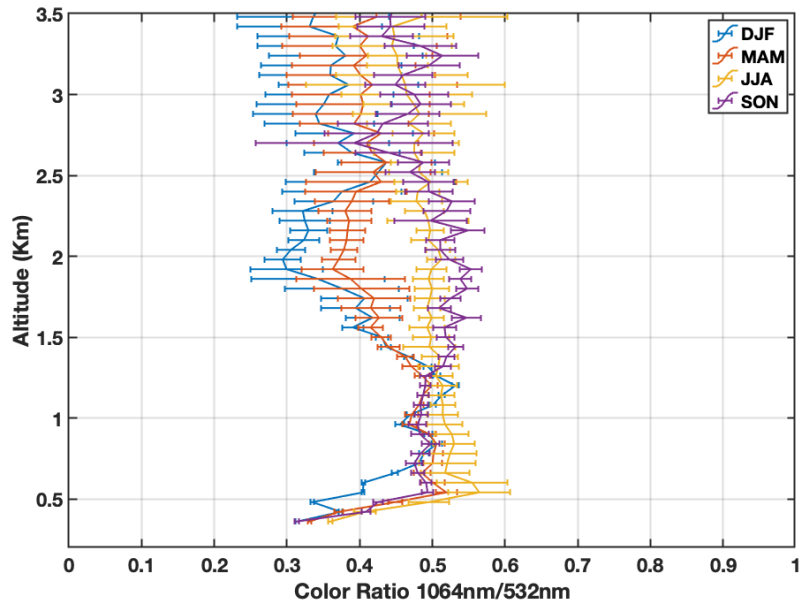
Figure 6. Color ratio for the different seasons obtained taking the ratio between the backscatter coefficient at 1064 nm and at 532 nm. Error bars are calculated considering the standard error (Eq. 1.)

3.2.1 Intense short-duration pollution events

In this section we focus on short episodes with high pollutant levels, proposing a methodology to filter and detect this kind of events. The median value of the seasonal profiles is computed to filter out intense short-lived episodes that are not climatologically significant. On the contrary, here we focus on the 95th percentile, instead of the median (50th), repeating the same analysis as in Section 3.2. Figure 7, shows a very different backscatter profile from Figure 4, especially for the cold season. The main characteristic of the winter profile is that it has an almost constant high aerosol concentration up to 3 Km. We analyzed individual events and found that the peaks can be attributed to Saharan dust outbreaks that occurred in February, starting from 2016. It seems that in recent years the meteorological circulation changed, bringing dust into Spain (Salvador et al., 2022) in winter. We also observed that these dust incursions have become not only more frequent but also more intense (Salvador et al., 2022). Several factors could be responsible for this change, including changes in global wind patterns, changing desertification rates in the Saharan regions, and broader climatic changes that influence air currents. Understanding these patterns is crucial not only for environmental and climatic studies, but also for public health, as higher levels of aerosols can affect air quality and respiratory health. The high-intense aerosol loading events were confirmed as dust outbreaks by the Barcelona Super Computing (BSC) Dream model reanalysis (Nickovic et al., 2001; Di Tomaso et al., 2022), while for the most intense episode, which occurred 3-4 February 2020, the Spanish Ministry of Environment (MITECO) sent a warning some days earlier.
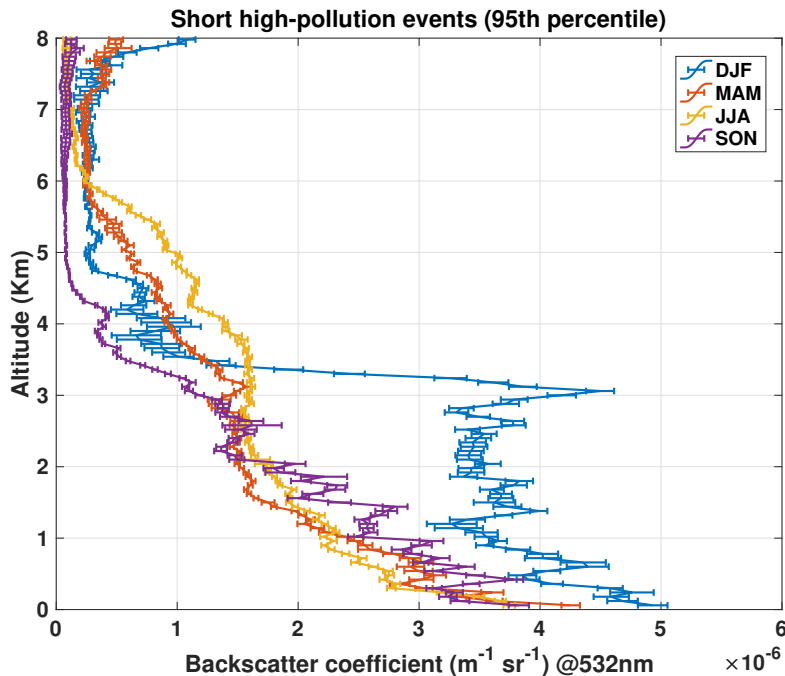
Figure 7. Vertically resolved 95th percentile backscattering profiles for DJF, MAM, JJA, and SON. Error bars are obtained by computing the standard error (value $\pm$ 1 σ_e; Eq. 1). The spatial resolution is constant and fixed at 60 m.]

3.2.2 Fine and Coarse mode

The vertically resolved color ratio accuracy is too low at 2.8 km, reaching errors of 100%. Seasonal signals can then be exploited
445 up to that altitude. Between 1 km and 2.8 km, the curves are well spread. CR profiles obtained through median averages indicate that the fine aerosol mode outweighs the coarse mode (resulting in fewer dust outbreaks). During DJF, a value greater than 0.5 can be observed at approximately 1 km, indicating the presence of a potential aerosol layer floating above the boundary layer, as previously observed from volume depolarization profiles. JJA and SON exhibit higher values compared to DJF and MAM, supporting the findings of the volume depolarization profiles for that altitude range.

450   To perform a more in-depth analysis, we analyzed the seasonal averages of the recovery of the Ångstrom exponent (microphysical variable) and AOD (optical variable) from the AERONET sunphotometer (columnar variables) as well as the concentrations of PM_{10}, $PM_{2.5}$ and PM_1 measured by in situ sensors located in conjunction with the lidar and the sunphotometer. The seasonal mean and standard deviation values obtained from the PM concentration measurements are summarized in Table 5, while Figure 8 shows all statistical values. PM_{10} concentrations shown in Figure 8 do not show any significant
455 seasonal trend, as the mean values remain relatively constant throughout the year. However, for $PM_{2.5}$, as illustrated in Figure 8, the concentrations drop by almost 20% during fall compared to winter. This trend is even more pronounced for PM1 (Figure 8), with a difference of 30% between summer and winter concentrations. Lower concentrations during summer and fall are as-

sociated with higher mixing layer height and convection. Both PM$_{2.5}$ and PM1 concentrations exhibit greater variability during summer, as shown in Figure 8. On the contrary, mean PM$_{10}$ concentrations remain relatively stable throughout the year, indi-

460 cating that heavier particles, such as marine salt, maintain constant levels at the surface. This characteristic is unique to coastal metropolitan cities, compared to continental regions such as the Po Valley, where PM$_{10}$ concentrations vary significantly with seasons (Landi et al., 2021).

Season	Group Count	PM$_{10}$	PM$_{2.5}$	PM$_1$	Std10	Std2.5	Std1
DJF	36674	26.5	18.5	14.3	22.9	14.0	11.9
MAM	37536	27.1	16.8	12.2	21.5	11.7	10.2
JJA	37536	24.6	14.6	10.0	17.2	8.3	6.9
SON	37128	23.7	15.6	11.2	17.2	10.8	9.0

Table 5. In situ PM concentration ($\mu g/m^3$) sensor measurements seasonal averaged
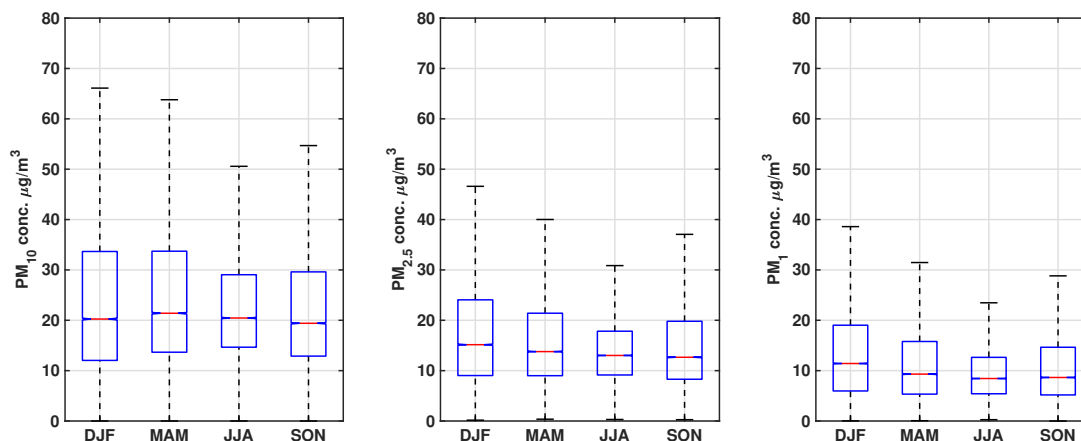
Figure 8. PM$_{10}$, PM$_{2.5}$ and PM$_1$ seasonal in-situ concentrations. The bottom and top of each box are the 25th and 75th percentiles of the sample, respectively. The red line at the center of each box represents the median of the sample. Whiskers are lines that extend above and under each box. Observations beyond the whisker length are marked as outliers (in red). Seasonal variability is more pronounced during summer for fine particles, with higher concentrations during winter. Coarse aerosols show a lower seasonal variability

Figure 10(a) displays the relative frequency distributions of AOD at the 440 nm wavelength. The results show that approximately 57% of the AOD values are below 0.2 and approximately 75% are below 0.3, while only 5% are above 0.4. Figure 9

465 shows the statistical parameters of the seasonal AOD for winter, spring, summer, and fall. The highest average value is observed during summer, while the lowest value is observed during winter. The highest variability in the data is observed during spring, which may be due to the influence of pollen (Sicard et al., 2021).
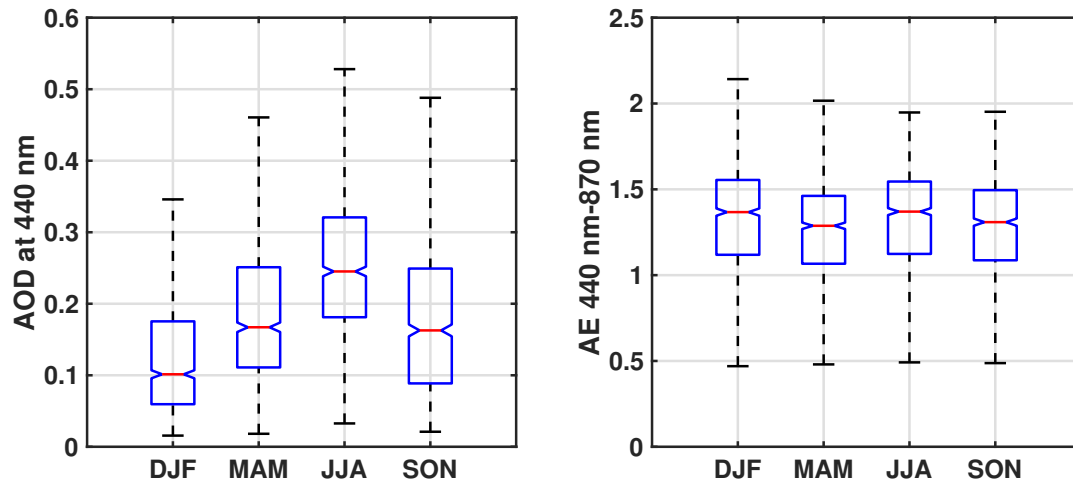
Figure 9. AERONET AOD and Ångstrom exponent seasonal boxplot. The bottom and top of each box are the 25th and 75th percentiles of the sample, respectively. The distance between the bottoms and tops of each box is the interquartile range. The red line in the center of each box represents the median of the sample. Whiskers are lines that extend above and below each box and correspond to the 95.4 percentile.

Season	Group Count	AOD	Ångstr. Exponent	StdAOD	StdÅng
DJF	1044	0.13	1.31	0.11	0.34
MAM	1098	0.20	1.25	0.12	0.32
JJA	1077	0.26	1.30	0.11	0.34
SON	927	0.18	1.27	0.12	0.30

Table 6. AERONET seasonal mean values and std for AOD and Ångstrom coefficient
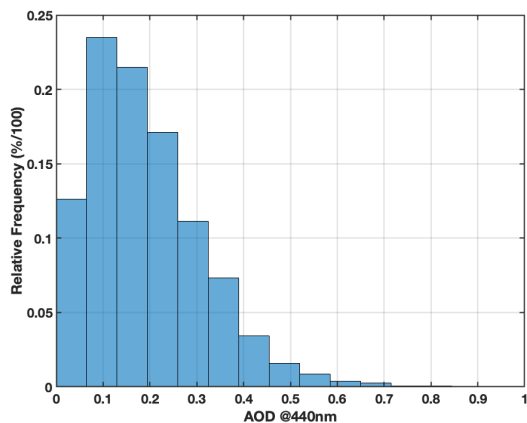
(a) Histogram AOD @440nm (b) Histogram Āngstrom @440nm-870nm
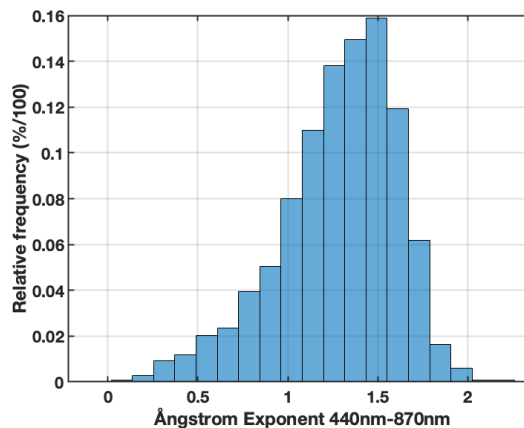
Figure 10. Relative frequency histogram of AOD (440 nm) and AE (440 nm-870 nm) from the UPC Barcelona AERONET station

Figure 10(b) shows a relative frequency histogram of AE (440–870 nm), which exhibits an asymmetrical shape with a left tail that extends far.

Most of the values, which represent approximately 55% of the cases, were between 1.2 and 1.6, consistent with the results of other urban/industrial areas. The presence of low AE values, less than 0.7, in approximately 8% of the data indicates that desert dust transport events in the Catalonia region are not uncommon. Intermediate values of AE are probably due to mixed cases, where a thin layer of desert dust is present at altitudes above the boundary layer and contributes to the effects of extinction, combined with those caused by suspended particle loading in the lower troposphere.

The statistical parameters of AE are shown in Figure 9 for the whole period. There is no high variability throughout the season. Figure 9 confirms that long-range transported Saharan dust has the same chance of occurring during all seasons, with AE almost constant throughout the seasons.

4   Conclusions and Future Perspectives

The present article discusses the impact of aerosols on human health, the environment, and climate in Barcelona, one of the largest metropolitan areas in the Mediterranean region. Aerosols are short-lived tiny particles suspended in the atmosphere and can come from both natural sources, such as volcano eruptions and dust outbreaks, and anthropogenic activities, such as burning fossil fuels. These particles can be carried by the wind from far away and can be found in high concentrations in certain areas. Breathing at high concentrations of aerosols can be harmful to human health, especially in vulnerable groups such as children and the elderly. It can cause respiratory problems, heart disease, and stroke. In contrast, the aerosols also modulate both the short-wave incoming solar radiation and the outgoing long-wave Earth radiation. Additionally, aerosols influence cloud formation and lifetime and impact precipitation. The latest Intergovernmental Panel on Climate Change (IPCC) highlighted

the need for aerosol research to reduce current uncertainty. For this reason, in this study, we quantitatively evaluated changes in the optical and microphysical properties of aerosols in Barcelona during the last 17 years through the seasonal Mann-Kendall test that analyzes long-term temporal trends in the concentrations of retrieved AOD, the Ångström exponent and PM_{10}, $PM_{2.5}$ and PM_1. The results highlight a sharp drop in PM concentration, AOD, and Ångström exponent from 2004 to 2020. These findings confirm that the emission reduction policies, implemented since 2004, were effective in improving air quality. From a climatological point of view, we also quantitatively assessed how the seasons influence the variability of the vertically resolved optical and microphysical properties of aerosols by lidar measurements obtained from the permanent station of the University Politecnica de Catalunya of the ACTRIS research infrastructure. We obtained four averaged profiles over 17 years of measurements, each representing the vertically resolved atmospheric aerosol backscatter profiles of each season.

The summer aerosol backscatter profile, averaged during June, July, and August, shows an exponential decay in the first km but also a long tail up to 5 km. This means that aerosol loading during this season can be found up to that altitude. On the contrary, the winter backscatter profile, which is obtained averaging the lidar observations in December, January, and February, shows a sharp exponential decay, with aerosols absent above 2.5 km. Both the spring aerosol backscatter profile, obtained averaging the lidar observations in March, April, and May, and the fall profile (averaged on September, October, and November) still show an exponential decay, but with a longer tail with detected aerosol presence up to 3 km in both cases. Spring and fall, and especially winter aerosol backscatter profiles, can be modeled by an exponential curve with a relative scale height H. In winter, for example, we have a scale height of H=0.61 km. This implies that 63% of the aerosol loading is capped below H. We further examined intense, short-duration, high concentration aerosol events and observed an increase in both the number of episodes and the intensity of dust outbreaks during winter, particularly in February, in the North-East of Spain. This corroborates the findings of (Salvador et al., 2022).

Analyzing the lidar seasonal averaged volume depolarization profiles, which show higher values for non-spherical aerosols such as Saharan dust, and the color ratio, defined as the ratio between the backscatter coefficient at 1064 nm and the backscatter coefficient at 532 nm wavelengths, higher for larger aerosol particles, we found that in winter dust outbreaks are likely to float over the boundary layer at an altitude of 1 km, while for the other seasons, dust can also descend into the boundary layer, being the profiles smoother. During the summer, most of the dust is capped at 2.5 km. This altitude probably corresponds to the height of the center of the Saharan dust layers. In summary, dust outbreaks occur throughout the season, but in winter dust floats over the boundary layer, whereas in the other seasons it can be embedded into it.

It is also important to emphasize the differences between ground-based in situ measurements (PM concentrations) and columnar (AOD and AE) and vertically resolved lidar observation, i.e., lidar data show a net increase above 3 km over the analyzed period in contrast to the yearly drop at surface of PM concentrations. Seasonal analysis also shows differences in aerosols at different altitudes that are not detectable by analyzing only the concentration of PM on the surface. This study then provides evidence that lidar observations are crucial to accurately evaluate aerosol dynamics. The ground-based observations do not capture the full picture.

This is the first study of this kind for the Iberian peninsula, and future research will evaluate whether the results found are confirmed in coastal and continental metropolitan regions of the Mediterranean, a climatic hotspot.

Author contributions. SL and TCL designed the study, SL, MS, AC performed the analysis, SL edited the first draft, FR edited and commented the first draft, FA provided data for lidar, AA, CR, XQ provided data for PM, and all of the authors assisted in interpreting the results and writing the paper.

525 *Competing interests.* At least one of the (co-)authors is a member of the editorial board of Atmospheric Chemistry and Physics

Acknowledgements. TEXT

,

References

Abshire, J. B., Riris, H., Allan, G. R., Weaver, C. J., Mao, J., Sun, X., Hasselbrack, W. E., Kawa, S. R., and Biraud, S.: Pulsed airborne lidar measurements of atmospheric CO2 column absorption, Tellus B: Chemical and Physical Meteorology, 62, 770–783, 2010.

Ackermann, J.: The extinction-to-backscatter ratio of tropospheric aerosol: A numerical study, Journal of atmospheric and oceanic technology, 15, 1043–1050, 1998.

Adler, C., Wester, P., Bhatt, I., Huggel, C., Insarov, G., Morecroft, M., Muccione, V., and Prakash, A.: Cross-Chapter Paper 5: Mountains, pp. 2273–2318, Cambridge University Press, Cambridge, UK and New York, USA, https://doi.org/10.1017/9781009325844.022.2273, 2022.

Alados-Arboledas, L., Müller, D., Guerrero-Rascado, J., Navas-Guzmán, F., Pérez-Ramírez, D., and Olmo, F.: Optical and microphysical properties of fresh biomass burning aerosol retrieved by Raman lidar, and star-and sun-photometry, Geophysical Research Letters, 38, 2011.

Ali, E., Cramer, W., Carnicer, J., Georgopoulou, E., Hilmi, N., Cozannet, G. L., and Lionello, P.: Cross-Chapter Paper 4: Mediterranean Region, pp. 2233–2272, Cambridge University Press, Cambridge, UK and New York, USA, https://doi.org/10.1017/9781009325844.021.2233, 2022.

Amiridis, V., Balis, D., Giannakaki, E., Stohl, A., Kazadzis, S., Koukouli, M., and Zanis, P.: Optical characteristics of biomass burning aerosols over Southeastern Europe determined from UV-Raman lidar measurements, Atmospheric Chemistry and Physics, 9, 2431–2440, 2009.

Ancellet, G., Pelon, J., Totems, J., Chazette, P., Bazureau, A., Sicard, M., Di Iorio, T., Dulac, F., and Mallet, M.: Long-range transport and mixing of aerosol sources during the 2013 North American biomass burning episode: analysis of multiple lidar observations in the western Mediterranean basin, Atmospheric Chemistry and Physics, 16, 4725–4742, 2016.

Ansmann, A., Riebesell, M., and Weitkamp, C.: Measurement of atmospheric aerosol extinction profiles with a Raman lidar, Optics letters, 15, 746–748, 1990.

Ansmann, A., Bösenberg, J., Chaikovsky, A., Comerón, A., Eckhardt, S., Eixmann, R., Freudenthaler, V., Ginoux, P., Komguem, L., Linné, H., et al.: Long-range transport of Saharan dust to northern Europe: The 11–16 October 2001 outbreak observed with EARLINET, Journal of Geophysical Research: Atmospheres, 108, 2003.

Ansmann, A., Tesche, M., Groß, S., Freudenthaler, V., Seifert, P., Hiebsch, A., Schmidt, J., Wandinger, U., Mattis, I., Müller, D., et al.: The 16 April 2010 major volcanic ash plume over central Europe: EARLINET lidar and AERONET photometer observations at Leipzig and Munich, Germany, Geophysical Research Letters, 37, 2010.

Basart, S., Pérez, C., Nickovic, S., Cuevas, E., and Baldasano, J. M.: Development and evaluation of the BSC-DREAM8b dust regional model over Northern Africa, the Mediterranean and the Middle East, Tellus B: Chemical and Physical Meteorology, https://doi.org/10.3402/tellusb.v64i0.18539, 2012.

Beer, A.: Bestimmung der Absorption des rothen Lichts in farbigen Flüssigkeiten, Annalen der Physik, 86, 78–88, 1852.

Bilal, M., Nichol, J. E., Nazeer, M., Shi, Y., Wang, L., Kumar, K. R., Ho, H. C., Mazhar, U., Bleiweiss, M. P., Qiu, Z., et al.: Characteristics of fine particulate matter (PM2. 5) over urban, suburban, and rural areas of Hong Kong, Atmosphere, 10, 496, 2019.

Bösenberg, J. and Matthias, V.: EARLINET: A European Aerosol Research Lidar Network to establish an aerosol climatology, 2003.

Browell, E., Ismail, S., and Grant, W.: Differential absorption lidar (DIAL) measurements from air and space, Applied Physics B, 67, 399–410, 1998.

Burton, S., Ferrare, R., Hostetler, C., Hair, J., Rogers, R., Obland, M., Butler, C., Cook, A., Harper, D., and Froyd, K.: Aerosol classification using airborne High Spectral Resolution Lidar measurements–methodology and examples, Atmospheric Measurement Techniques, 5, 73–98, 2012.

Cairo, F., Di Donfrancesco, G., Adriani, A., Pulvirenti, L., and Fierli, F.: Comparison of various linear depolarization parameters measured by lidar, Applied Optics, 38, 4425–4432, 1999.

Campbell, J. R., Lolli, S., Lewis, J. R., Gu, Y., and Welton, E. J.: Daytime cirrus cloud top-of-the-atmosphere radiative forcing properties at a midlatitude site and their global consequences, Journal of Applied Meteorology and Climatology, 55, 1667–1679, 2016.

Campbell, J. R., Peterson, D. A., Marquis, J. W., Fochesatto, G. J., Vaughan, M. A., Stewart, S. A., Tackett, J. L., Lolli, S., Lewis, J. R., Oyola, M. I., and Welton, E. J.: Unusually Deep Wintertime Cirrus Clouds Observed over the Alaskan Subarctic, Bulletin of the American Meteorological Society, 99, 27–32, https://doi.org/10.1175/BAMS-D-17-0084.1, 2018.

Carnuth, W., Kempfer, U., and Trickl, T.: Highlights of the tropospheric lidar studies at IFU within the TOR project, Tellus B: Chemical and Physical Meteorology, 54, 163–185, 2002.

Charron, A., Harrison, R. M., Moorcroft, S., and Booker, J.: Quantitative interpretation of divergence between PM10 and PM2. 5 mass measurement by TEOM and gravimetric (Partisol) instruments, Atmospheric Environment, 38, 415–423, 2004.

Ciofini, M., Lapucci, A., and Lolli, S.: Diffractive optical components for high power laser beam sampling, Journal of Optics A: Pure and Applied Optics, 5, 186, 2003.

Cohen, J. B. and Wang, C.: Estimating global black carbon emissions using a top-down Kalman Filter approach, Journal of Geophysical Research: Atmospheres, 119, 307–323, 2014.

Cramer, W., Guiot, J., Fader, M., Garrabou, J., Gattuso, J.-P., Iglesias, A., Lange, M. A., Lionello, P., Llasat, M. C., Paz, S., et al.: Climate change and interconnected risks to sustainable development in the Mediterranean, Nature Climate Change, 8, 972–980, 2018.

Crosier, J., Allan, J., Coe, H., Bower, K., Formenti, P., and Williams, P.: Chemical composition of summertime aerosol in the Po Valley (Italy), northern Adriatic and Black Sea, Quarterly Journal of the Royal Meteorological Society: A journal of the atmospheric sciences, applied meteorology and physical oceanography, 133, 61–75, 2007.

D'Amico, G., Amodeo, A., Baars, H., Binietoglou, I., Freudenthaler, V., Mattis, I., Wandinger, U., and Pappalardo, G.: EARLINET Single Calculus Chain–overview on methodology<? xmltex\break?> and strategy, Atmospheric Measurement Techniques, 8, 4891–4916, 2015.

D'Amico, G., Amodeo, A., Mattis, I., Freudenthaler, V., and Pappalardo, G.: EARLINET Single Calculus Chain–technical–Part 1: Preprocessing of raw lidar data, Atmospheric Measurement Techniques, 9, 491–507, 2016.

Di Tomaso, E., Escribano, J., Basart, S., Ginoux, P., Macchia, F., Barnaba, F., Benincasa, F., Bretonnière, P.-A., Buñuel, A., Castrillo, M., et al.: The MONARCH high-resolution reanalysis of desert dust aerosol over Northern Africa, the Middle East and Europe (2007–2016), Earth system science data, 14, 2785–2816, 2022.

Dubovik, O., Holben, B. N., Eck, T. F., Smirnov, A., Kaufman, Y. J., King, M. D., Tanré, D., and Slutsker, I.: Variability of absorption and optical properties of key aerosol types observed in worldwide locations, Journal of the atmospheric sciences, 59, 590–608, 2002.

Eck, T. F. and Holben, B. N.: Wavelength dependence of the optical depth of biomass burning, urban, and desert dust aerosols, Journal of Geophysical Research: Atmospheres, 104, 31 333–31 349, 1999.

Ehret, G., Bousquet, P., Pierangelo, C., Alpers, M., Millet, B., Abshire, J. B., Bovensmann, H., Burrows, J. P., Chevallier, F., Ciais, P., et al.: MERLIN: A French-German space lidar mission dedicated to atmospheric methane, Remote Sensing, 9, 1052, 2017.

Evan, A. T., Flamant, C., Gaetani, M., and Guichard, F.: The past, present and future of African dust, Nature, 531, 493–495, 2016.

Fan, H., Zhao, C., Yang, Y., and Yang, X.: Spatio-temporal variations of the PM2. 5/PM10 ratios and its application to air pollution type classification in China, Frontiers in Environmental Science, 9, 692 440, 2021.

Ferrare, R., Turner, D., Clayton, M., Schmid, B., Redemann, J., Covert, D., Elleman, R., Ogren, J., Andrews, E., Goldsmith, J. E., et al.: Evaluation of daytime measurements of aerosols and water vapor made by an operational Raman lidar over the Southern Great Plains, Journal of Geophysical Research: Atmospheres, 111, 2006.

Freudenthaler, V., Esselborn, M., Wiegner, M., Heese, B., Tesche, M., Ansmann, A., Müller, D., Althausen, D., Wirth, M., Fix, A., et al.: Depolarization ratio profiling at several wavelengths in pure Saharan dust during SAMUM 2006, Tellus B: Chemical and Physical Meteorology, 61, 165–179, 2009.

Giles, D. M., Sinyuk, A., Sorokin, M. G., Schafer, J. S., Smirnov, A., Slutsker, I., Eck, T. F., Holben, B. N., Lewis, J. R., Campbell, J. R., et al.: Advancements in the Aerosol Robotic Network (AERONET) Version 3 database–automated near-real-time quality control algorithm with improved cloud screening for Sun photometer aerosol optical depth (AOD) measurements, Atmospheric Measurement Techniques, 12, 169–209, 2019.

Giovanni: Global Modeling and Assimilation Office (GMAO) MERRA-2 Monthly mean Time-averaged Single-Level, Assimilation Aerosol Diagnostics V5.12.4 Greenbelt MD USA, Goddard Earth Sciences Data and Information Services Center (GES DISC), https://doi.org/10.5067/FH9A0MLJPC7N, 2015.

Gross, S., Freudenthaler, V., Wiegner, M., Gasteiger, J., Geiss, A., and Schnell, F.: Dual-wavelength linear depolarization ratio of volcanic aerosols: Lidar measurements of the Eyjafjallajökull plume over Maisach, Germany, Atmospheric Environment, 48, 85–96, 2012.

Grund, C. J. and Eloranta, E. W.: University of Wisconsin high spectral resolution lidar, Optical Engineering, 30, 6–12, 1991.

Guerrero-Rascado, J., Ruiz, B., and Alados-Arboledas, L.: Multi-spectral Lidar characterization of the vertical structure of Saharan dust aerosol over southern Spain, Atmospheric Environment, 42, 2668–2681, 2008.

Haarig, M., Ansmann, A., Baars, H., Jimenez, C., Veselovskii, I., Engelmann, R., and Althausen, D.: Depolarization and lidar ratios at 355, 532, and 1064 nm and microphysical properties of aged tropospheric and stratospheric Canadian wildfire smoke, 2018.

Hess, M., Koepke, P., and Schult, I.: Optical properties of aerosols and clouds: The software package OPAC, Bulletin of the American meteorological society, 79, 831–844, 1998.

Hirsch, R. M., Slack, J. R., and Smith, R. A.: Techniques of trend analysis for monthly water quality data, Water resources research, 18, 107–121, 1982.

Holben, B. N., Eck, T. F., Slutsker, I. a., Tanre, D., Buis, J., Setzer, A., Vermote, E., Reagan, J. A., Kaufman, Y., Nakajima, T., et al.: AERONET—A federated instrument network and data archive for aerosol characterization, Remote sensing of environment, 66, 1–16, 1998.

Huang, T., Yang, Y., O'Connor, E. J., Lolli, S., Haywood, J., Osborne, M., Cheng, J. C.-H., Guo, J., and Yim, S. H.-L.: Influence of a weak typhoon on the vertical distribution of air pollution in Hong Kong: A perspective from a Doppler LiDAR network, Environmental Pollution, 276, 116 534, 2021.

Kumar, D., Rocadenbosch, F., Sicard, M., Comeron, A., Muñoz, C., Lange, D., Tomás, S., and Gregorio, E.: Six-channel polychromator design and implementation for the UPC elastic/Raman LIDAR, in: Lidar Technologies, Techniques, and Measurements for Atmospheric Remote Sensing VII, vol. 8182, pp. 185–194, SPIE, 2011.

Landi, T. C., Bonasoni, P., Brunetti, M., Campbell, J. R., Marquis, J. W., Di Girolamo, P., and Lolli, S.: Aerosol Direct Radiative Effects under Cloud-Free Conditions over Highly-Polluted Areas in Europe and Mediterranean: A Ten-Years Analysis (2007–2016), Remote Sensing, 13, https://doi.org/10.3390/rs13152933, 2021.

Lautenbacher, C.: The global earth observation system of systems (GEOSS), in: 2005 IEEE International Symposium on Mass Storage Systems and Technology, pp. 47–50, IEEE, 2005.

Levy, R. C., Mattoo, S., Munchak, L. A., Remer, L. A., Sayer, A. M., Patadia, F., and Hsu, N. C.: Algorithm for remote sensing of tropospheric aerosol over dark targets from MODIS: Collections 005 and 051, Atmospheric Measurement Techniques, 3, 1187–1211, 2010.

Lewis, S. C., King, A. D., Perkins-Kirkpatrick, S. E., and Mitchell, D. M.: Regional hotspots of temperature extremes under 1.5 C and 2 C of global mean warming, Weather and Climate Extremes, 26, 100 233, 2019.

Liu, B., Ma, Y., Gong, W., and Zhang, M.: Observations of aerosol color ratio and depolarization ratio over Wuhan, Atmospheric Pollution Research, 8, 1113–1122, 2017.

Lolli, S., Welton, E., and Sauvage, L.: EZ LIDAR™ measurement results in the frame of Indian Monsoon TIGER-Z NASA campaign, in: Proc. of SPIE Vol, vol. 7111, pp. 71 110I–1, 2008.

Lolli, S., Sauvage, L., Loaec, S., and Lardier, M.: EZ Lidar™: A new compact autonomous eye-safe scanning aerosol Lidar for extinction measurements and PBL height detection. Validation of the performances against other instruments and intercomparison campaigns, Óptica pura y aplicada, 44, 33–41, 2011.

Lolli, S., Delaval, A., Loth, C., Garnier, A., and Flamant, P.: 0.355-micrometer direct detection wind lidar under testing during a field campaign in consideration of ESA's ADM-Aeolus mission, Atmospheric Measurement Techniques, 6, 3349–3358, 2013.

Lolli, S., Campbell, J. R., Lewis, J. R., Gu, Y., Marquis, J. W., Chew, B. N., Liew, S.-C., Salinas, S. V., and Welton, E. J.: Daytime Top-of-the-Atmosphere Cirrus Cloud Radiative Forcing Properties at Singapore, Journal of Applied Meteorology and Climatology, 56, 1249–1257, 2017.

Lolli, S., Khor, W. Y., Matjafri, M. Z., and Lim, H. S.: Monsoon season quantitative assessment of biomass burning clear-sky aerosol radiative effect at surface by ground-based lidar observations in Pulau Pinang, Malaysia in 2014, Remote Sensing, 11, 2660, 2019.

Mamouri, R.-E. and Ansmann, A.: Fine and coarse dust separation with polarization lidar, Atmospheric Measurement Techniques, 7, 3717–3735, 2014.

Mamouri, R.-E., Ansmann, A., Nisantzi, A., Kokkalis, P., Schwarz, A., and Hadjimitsis, D.: Low Arabian dust extinction-to-backscatter ratio, Geophysical Research Letters, 40, 4762–4766, 2013.

Marinou, E., Amiridis, V., Binietoglou, I., Tsikerdekis, A., Solomos, S., Proestakis, E., Konsta, D., Papagiannopoulos, N., Tsekeri, A., Vlastou, G., et al.: Three-dimensional evolution of Saharan dust transport towards Europe based on a 9-year EARLINET-optimized CALIPSO dataset, Atmospheric Chemistry and Physics, 17, 5893–5919, 2017.

Mattis, I., Siefert, P., Müller, D., Tesche, M., Hiebsch, A., Kanitz, T., Schmidt, J., Finger, F., Wandinger, U., and Ansmann, A.: Volcanic aerosol layers observed with multiwavelength Raman lidar over central Europe in 2008–2009, Journal of Geophysical Research: Atmospheres, 115, 2010.

Mazzola, M., Lanconelli, C., Lupi, A., Busetto, M., Vitale, V., and Tomasi, C.: Columnar aerosol optical properties in the Po Valley, Italy, from MFRSR data, Journal of Geophysical Research: Atmospheres, 115, 2010.

Mona, L., Amodeo, A., Pandolfi, M., and Pappalardo, G.: Saharan dust intrusions in the Mediterranean area: Three years of Raman lidar measurements, Journal of Geophysical Research: Atmospheres, 111, 2006.

Mueller, D., Uibel, S., Takemura, M., Klingelhoefer, D., and Groneberg, D. A.: Ships, ports and particulate air pollution-an analysis of recent studies, Journal of Occupational Medicine and Toxicology, 6, 1–6, 2011.

675 Müller, D., Mattis, I., Wandinger, U., Ansmann, A., Althausen, D., and Stohl, A.: Raman lidar observations of aged Siberian and Canadian forest fire smoke in the free troposphere over Germany in 2003: Microphysical particle characterization, Journal of Geophysical Research: Atmospheres, 110, 2005.

Navas-Guzmán, F., Müller, D., Bravo-Aranda, J., Guerrero-Rascado, J., Granados-Muñoz, M., Pérez-Ramírez, D., Olmo, F., and Alados-Arboledas, L.: Eruption of the Eyjafjallajökull Volcano in spring 2010: Multiwavelength Raman lidar measurements of sulphate particles

680 in the lower troposphere, Journal of Geophysical Research: Atmospheres, 118, 1804–1813, 2013.

Nicholls, R. J., Wong, P. P., Burkett, V., Woodroffe, C. D., and Hay, J.: Climate change and coastal vulnerability assessment: scenarios for integrated assessment, 2008.

Nickovic, S., Kallos, G., Papadopoulos, A., and Kakaliagou, O.: A model for prediction of desert dust cycle in the atmosphere, Journal of Geophysical Research: Atmospheres, 106, 18 113–18 129, 2001.

685 Nisantzi, A., Mamouri, R.-E., Ansmann, A., and Hadjimitsis, D.: Injection of mineral dust into the free troposphere during fire events observed with polarization lidar at Limassol, Cyprus, Atmospheric Chemistry and Physics, 14, 12 155–12 165, 2014.

Nisantzi, A., Mamouri, R.-E., Ansmann, A., Schuster, G., and Hadjimitsis, D. G.: Middle East versus Saharan dust extinction-to-backscatter ratios, Atmospheric Chemistry and Physics, 15, 7071–7084, 2015.

Papayannis, A., Amiridis, V., Mona, L., Tsaknakis, G., Balis, D., Bösenberg, J., Chaikovski, A., De Tomasi, F., Grigorov, I., Mattis, I., et al.:

690 Systematic lidar observations of Saharan dust over Europe in the frame of EARLINET (2000–2002), Journal of Geophysical Research: Atmospheres, 113, 2008.

Papayannis, A., Mamouri, R., Amiridis, V., Giannakaki, E., Veselovskii, I., Kokkalis, P., Tsaknakis, G., Balis, D., Kristiansen, N., Stohl, A., et al.: Optical properties and vertical extension of aged ash layers over the Eastern Mediterranean as observed by Raman lidars during the Eyjafjallajökull eruption in May 2010, Atmospheric Environment, 48, 56–65, 2012.

695 Pappalardo, G., Amodeo, A., Mona, L., Pandolfi, M., Pergola, N., and Cuomo, V.: Raman lidar observations of aerosol emitted during the 2002 Etna eruption, Geophysical Research Letters, 31, 2004.

Pappalardo, G., Wandinger, U., Mona, L., Hiebsch, A., Mattis, I., Amodeo, A., Ansmann, A., Seifert, P., Linné, H., Apituley, A., et al.: EARLINET correlative measurements for CALIPSO: First intercomparison results, Journal of Geophysical Research: Atmospheres, 115, 2010.

700 Pappalardo, G., Mona, L., D'Amico, G., Wandinger, U., Adam, M., Amodeo, A., Ansmann, A., Apituley, A., Alados Arboledas, L., Balis, D., et al.: Four-dimensional distribution of the 2010 Eyjafjallajökull volcanic cloud over Europe observed by EARLINET, Atmospheric Chemistry and Physics, 13, 4429–4450, 2013.

Pappalardo, G., Amodeo, A., Apituley, A., Comeron, A., Freudenthaler, V., Linné, H., Ansmann, A., Bösenberg, J., D'Amico, G., Mattis, I., , et al.: EARLINET: towards an advanced sustainable European aerosol lidar network, Atmospheric Measurement Techniques, 7,

705 2389–2409, 2014.

Pope III, C. A. and Dockery, D. W.: Health effects of fine particulate air pollution: lines that connect, Journal of the air & waste management association, 56, 709–742, 2006.

Qin, K., Lu, L., Liu, J., He, Q., Shi, J., Deng, W., Wang, S., and Cohen, J. B.: Model-free daily inversion of NOx emissions using TROPOMI (MCMFE-NOx) and its uncertainty: Declining regulated emissions and growth of new sources, Remote Sensing of Environment, 295,

710 113 720, 2023.

Reche, C., Perez, N., Alastuey, A., Cots, N., Pérez, E., and Querol, X.: 2011–2020 trends of urban and regional ammonia in and around Barcelona, NE Spain, Chemosphere, 304, 135 347, 2022.

Reichardt, J., Wandinger, U., Klein, V., Mattis, I., Hilber, B., and Begbie, R.: RAMSES: German Meteorological Service autonomous Raman lidar for water vapor, temperature, aerosol, and cloud measurements, Applied optics, 51, 8111–8131, 2012.

715 Rodríguez-Gómez, A., Muñoz-Porcar, C., Zenteno-Hernández, J.-A., Comerón, A., Dios, F., Sicard, M., Gil-Díaz, C., Oliveira, D. C. F., and Mandal, C.: Use of pure rotational Raman channels for lidar measurement of aerosol extinction coefficient: the EARLINET/ACTRIS Barcelona station experience, in: Remote Sensing of Clouds and the Atmosphere XXVII, vol. 12265, pp. 60–70, SPIE, 2022.

Salvador, P., Pey, J., Pérez, N., Querol, X., and Artíñano, B.: Increasing atmospheric dust transport towards the western Mediterranean over 1948–2020, npj Climate and Atmospheric Science, 5, 34, 2022.

720 Sicard, M., Molero, F., Guerrero-Rascado, J. L., Pedrós, R., Expósito, F. J., Córdoba-Jabonero, C., Bolarín, J. M., Comerón, A., Rocadenbosch, F., Pujadas, M., et al.: Aerosol LiDAR intercomparison in the framework of SPALINET—The Spanish LiDAR network: Methodology and results, IEEE transactions on geoscience and remote sensing, 47, 3547–3559, 2009.

Sicard, M., Rocadenbosch, F., Reba, M., Comerón, A., Tomás, S., García-Vízcaino, D., Batet, O., Barrios, R., Kumar, D., and Baldasano, J.: Seasonal variability of aerosol optical properties observed by means of a Raman lidar at an EARLINET site over Northeastern Spain,
725   Atmospheric Chemistry and Physics, 11, 175–190, 2011.

Sicard, M., Guerrero-Rascado, J. L., Navas-Guzmán, F., Preißler, J., Molero, F., Tomás, S., Bravo-Aranda, J. A., Comerón, A., Rocadenbosch, F., Wagner, F., et al.: Monitoring of the Eyjafjallajökull volcanic aerosol plume over the Iberian Peninsula by means of four EARLINET lidar stations, Atmospheric Chemistry and Physics, 12, 3115–3130, 2012.

Sicard, M., Jorba, O., Ho, J. J., Izquierdo, R., De Linares, C., Alarcón, M., Comerón, A., and Belmonte, J.: Measurement report: Charac-
730   terization of the vertical distribution of airborne Pinus pollen in the atmosphere with lidar-derived profiles–a modeling case study in the region of Barcelona, NE Spain, Atmospheric Chemistry and Physics, 21, 17 807–17 832, 2021.

Smirnov, A., Holben, B. N., Kaufman, Y. J., Dubovik, O., Eck, T. F., Slutsker, I., Pietras, C., and Halthore, R. N.: Optical properties of atmospheric aerosol in maritime environments, Journal of the Atmospheric Sciences, 59, 501–523, 2002.

Stocker, T.: Climate change 2013: the physical science basis: Working Group I contribution to the Fifth assessment report of the Intergov-
735   ernmental Panel on Climate Change, Cambridge university press, 2014.

Tanré, D., Buis, J., Setzer, A., Vermote, E., Kaufman, Y., Nakajima, T., et al.: AERONET—A federated instrument network and data archive for aerosol characterization, Remote sensing of environment, 66, 1–16, 1998.

Tosca, M. G., Campbell, J., Garay, M., Lolli, S., Seidel, F. C., Marquis, J., and Kalashnikova, O.: Attributing Accelerated Summertime Warming in the Southeast United States to Recent Reductions in Aerosol Burden: Indications from Vertically-Resolved Observations,
740   Remote Sensing, 9, 674, 2017.

Vaughan, M.: Algorithm for retrieving lidar ratios at 1064 nm from space-based lidar backscatter data, in: Laser radar technology for remote sensing, vol. 5240, pp. 104–115, SPIE, 2004.

Von Storch, H. and Zwiers, F. W.: Statistical analysis in climate research, Cambridge university press, 2002.

Wang, S., Wang, X., Cohen, J. B., and Qin, K.: Inferring polluted Asian absorbing aerosol properties using decadal scale AERONET mea-
745   surements and a MIE model, Geophysical Research Letters, 48, e2021GL094 300, 2021.

Wang, X., Boselli, A., D'Avino, L., Pisani, G., Spinelli, N., Amodeo, A., Chaikovsky, A., Wiegner, M., Nickovic, S., Papayannis, A., et al.: Volcanic dust characterization by EARLINET during Etna's eruptions in 2001–2002, Atmospheric environment, 42, 893–905, 2008.

Whiteman, D. N.: Examination of the traditional Raman lidar technique. I. Evaluating the temperature-dependent lidar equations, Applied Optics, 42, 2571–2592, 2003.

Wiegner, M., Gasteiger, J., Groß, S., Schnell, F., Freudenthaler, V., and Forkel, R.: Characterization of the Eyjafjallajökull ash-plume: Potential of lidar remote sensing, Physics and Chemistry of the Earth, Parts A/B/C, 45, 79–86, 2012.

Xue, J., Zong, L., Yang, Y., Bi, X., Zhang, Y., and Zhao, M.: Diurnal and interannual variations of canopy urban heat island (CUHI) effects over a mountain–valley city with a semi-arid climate, Urban Climate, 48, 101 425, 2023.

Yang, Y., Fan, S., Wang, L., Gao, Z., Zhang, Y., Zou, H., Miao, S., Li, Y., Huang, M., Yim, S. H. L., et al.: Diurnal evolution of the wintertime boundary layer in urban Beijing, China: Insights from Doppler Lidar and a 325-m meteorological tower, Remote Sensing, 12, 3935, 2020.

Yue, S., Pilon, P., and Cavadias, G.: Power of the Mann–Kendall and Spearman's rho tests for detecting monotonic trends in hydrological series, Journal of hydrology, 259, 254–271, 2002.

Zenteno-Hernández, J. A., Comerón, A., Rodríguez-Gómez, A., Muñoz-Porcar, C., D'Amico, G., and Sicard, M.: A comparative analysis of aerosol optical coefficients and their associated errors retrieved from pure-rotational and vibro-rotational raman lidar signals, Sensors, 21, 1277, 2021.